Received January 22, 2022, accepted January 29, 2022, date of publication January 31, 2022, date of current version February 4, 2022.

Digital Object Identifier 10.1109/ACCESS.2022.3148246

Optimization and Improvement of Advanced Nonoverlapping Induction Machines for EVs/HEVs

T. GUNDOGDU[1,2], (Member, IEEE), Z. Q. ZHU[1], (Fellow, IEEE), AND J. C. MIPO[3], (Member, IEEE)

[1]Department of Electronic and Electrical Engineering, The University of Sheffield, Sheffield S10 3JD, U.K.
[2]Department of Electrical and Electronic Engineering, Hakkari University, 30000 Hakkâri, Turkey
[3]Valeo Powertrain Electric Systems, 94017 Créteil, France

Corresponding author: Z. Q. Zhu (z.q.zhu@sheffield.ac.uk)

This work was supported by Valeo Powertrain Electric Systems, Créteil, France.

ABSTRACT This paper presents a comprehensive design optimization and performance improvement guidelines for induction machines (IMs) having advanced nonoverlapping windings (ANWs). The effectiveness of various optimization approaches, such as individual optimization and single- and multi-objective global optimization using the Genetic Algorithm (GA), has been studied. To minimize the potential drawbacks of high bar copper loss, high torque ripple, and low power at high speed due to high magnet-motive force (MMF) harmonics of nonoverlapping windings (NWs), two different performance improvement approaches have been utilized: (a) to redesign the rotor structure to reduce the parasitic effects such as torque ripple and additional bar copper losses due to air-gap flux density harmonics; (b) to increase the stack length to improve the torque at the constant-power region. It has been revealed that the proposed ANW IMs with bridges in their rotor openings, particularly with u-shaped bridges, show better performance in terms of torque ripple, bar copper loss, and bar current density. By using the proposed design method, an advanced IM (AIM) can achieve a 5.3% higher efficiency with ∼34% shorter total axial length, compared to its conventional IM (CIM) counterpart with integer-slot distributed windings (ISDWs). A time-stepping 2-D finite element analysis (FEA) based nonlinear magnetic field solution program has been employed to perform all the parametric analyses, optimizations, and evaluate the optimal solutions and improved designs. Moreover, in order to show the reliability of the FEA predictions performed in this study, the FEA predictions of globally optimized CIM are validated by experimental measurements.

INDEX TERMS Electromagnetic performance, flux-weakening, genetic algorithm, global optimization, individual optimization, induction machine, parameter and objective justifications, nonoverlapping winding, squirrel-cage.

NOMENCLATURE

A_s	Stator slot area
B_g	Average air-gap flux density
D_{so}	Stator outer diameter
G	Sub-goal number
I_s	Phase current
J_r	Rotor bar current density
J_s	Stator current density
N_c	Number of coils
N_j	Number of frequencies for the j^{th} sub-goal
N_t	Number of turns per coil
P	Pole number
P_{out}	Active power
$P_{rcu(Max\_S_{bar})}$	Maximum rotor bar loss obtained in case of maximum rotor bar surface area
$P_{rcu(Max\_Cost)}$	Rotor bar loss corresponding to maximum cost
$P_{rcu(Min\_Cost)}$	Rotor bar loss corresponding to minimum cost
$P_{rcu(Min\_Sbar)}$	Minimum rotor bar loss obtained in case of minimum rotor bar surface areas
$P_{scu(MOGO12)}$	Stator slot copper loss obtained from the SOGO solution
$P_{scu(SOGO-R1)}$	Stator slot copper loss obtained from the SOGO solution in case of maximum stator current density restriction
$P_{scu(SOGO-R2)}$	Stator slot copper loss obtained from the SOGO solution in case of maximum stator copper loss restriction

The associate editor coordinating the review of this manuscript and approving it for publication was R. K. Saket.

R	Rotor slot number
R_{phase}	Phase resistance
S	Stator slot number
S_{out}	Apparent power
T	Electromagnetic torque
a	Parallel branch number
a_c	Electric loading
b_{ror}	Rotor slot opening ratio
b_{rr}	Rotor slot width ratio
b_s	Stator slot width ratio
b_{ser}	Stator slot width ratio for zig-zag stator structure
b_{sor}	Stator slot opening ratio
e_i	Error value of the i^{th} iteration
e_{ji}	Error contribution from the j^{th} sub-goal at the i^{th} frequency
h_r	Rotor yoke thickness ratio
h_s	Stator yoke thickness ratio
h_{ser}	Stator yoke thickness ratio for zig-zag stator structure
k	Positive integer
k_c	Copper loss coefficient
k_f	Slot fill factor
k_{wp}	Fundamental winding factor
ℓ	Active stack length
ℓ_a	Total axial length
n_r	Rotor speed
n_t	Overlay number
w_i	Absolute weight value of the i^{th} iteration
w_j	Weight factor related with the j^{th} sub-goal
y_c	Coil pitch number
λ_s	Stator split ratio
ρ_{cu}	Resistivity of the copper
ω	Angular speed

I. INTRODUCTION

Electric and hybrid electric vehicles (EVs/HEVs) require electrical machines with high-torque density, which is always a challenge. One of the practical solutions is to reduce the axial length of end-windings by using conventional short-pitch (overlapping) windings or one slot pitch concentrated (nonoverlapping) windings [1]–[9]. Thus, the torque density can be further enhanced by replacing the end-windings with the active lamination stack within the same machine space envelop. Compared to short-pitch overlapping windings, the one slot pitch concentrated windings are characterized with high-space magnetomotive force (MMF) harmonics which result in undesirable effects on electric machines, such as increased localized core saturation, stator iron losses, and eddy current loss in the rotor, particularly in rotor conductors or magnets [4]–[12]. Therefore, conventional nonoverlapping winding (NW) configuration requires structural modifications as presented in [5]–[11] to eliminate or reduce the MMF harmonic content.

In [5], an outer rotor squirrel cage induction machine (IM) having dual stator slot layers and three-layer NWs with varying turns per coil and a skewed rotor is proposed to obtain a high-torque density. However, a substantial drop in efficiency results due to the decreased fundamental winding factor and increased core and rotor bar copper losses. An improved FSCW topology with a dual slot-layer stator structure having 4-layer shifted windings with a different number of turns per coil is presented in [6]. Although the proposed winding topology has low MMF harmonic content and shorter end-winding length, it has serious drawbacks such as applicability only to low poles and a very low fundamental winding factor. A FSCW configuration with star and delta windings having different numbers of turns per coil is proposed in [7] to minimize the MMF harmonic content and ohmic losses. However, it has resulted in a relatively low fundamental winding factor and a high THD of MMF. In [8], in order to improve the efficiency and reduce the length of end-windings, a single-layer toroidal winding topology is employed for an IM. Although no information about the winding factor and MMF harmonics is presented, lower winding resistance according to its conventional counterpart is measured. A double-layer NW is proposed in [9] to reduce the MMF spatial harmonics and also AC losses of synchronous permanent magnet machine having the 2^{nd} generation high-temperature superconductor (2G HTS) armature. In [10], a similar winding arrangement proposed in [9] is utilized for an IM having two-layer advanced nonoverlapping windings (ANWs) and unconventional stator structure, whose slots are utilized to reduce the core saturation and leakage flux, to improve the torque density and efficiency. It is concluded that compared to its conventional counterpart, a 25% shorter IM having maintained torque, output power, and efficiency is achieved.

In order to demonstrate the originality and effectiveness of the proposed winding topology, a comparison of some key design and performance characteristics with existing nonoverlapping winding methodologies is given in Table 1. As can be seen from this table, compared to the proposed topology, the main drawbacks of the existing topologies can be listed as follows.

1. Low fundamental winding factor → Low average torque and hence low torque density (low TpV);
2. Relatively high MMF harmonic content → High rotor losses and hence relatively low efficiency;
3. High number of winding layers → Low slot fill factor;
4. Difficulty in winding assembling.

In [10], it is also shown that thanks to the ANW topology, either the electromagnetic performance can be improved, or the total axial length can be reduced significantly without sacrificing the torque and efficiency. Moreover, a detailed design guideline for IMs having ANWs, and influence of major design parameters on both steady-state (SS) and flux-weakening (FW) performance characteristics have been reported in [11]. In this study, it is aimed to (a) optimize these advanced IMs (AIMs) by using different optimization approaches and (b) further improve the performance charac-

teristics by reducing the power losses and enlarging the speed range at constant power region.

Since the invention of the computer, traditional optimization methods have been used to design IMs [12], and the subject of optimal design of IM is gaining a lot of attention. Numerous studies on the optimization of conventional IMs with wound field or squirrel-cage rotors have been published in literature. These studies can be categorized into the following groups:

(a) *Optimization of design;*
   - Cost: volume, material type, weight, etc. [13], [14];
   - Performance: efficiency, torque, air-gap flux, acoustic noise, torque ripple, etc. [12], [16];
   - Cost and performance: [17]–[21].

(b) *Utilization or comparison of several optimization algorithms*: [22]–[24];

(c) *Optimization of control algorithms* [25], [26].

One of the very first optimization study on an IM is presented in [13]. Design optimization of an IM is investigated from the viewpoints of the consumer and national economy. In order to reduce the overall cost of the IM, consumer-optimized parameters are analysed [13]. In [14], a mathematical programming, based on sequential unconstrained minimization technique (SUMT), has been applied for the optimization of IM design parameters in order to minimize the material cost by considering the pull-out torque, starting torque, etc. Moreover, the utilized optimization method SUMT has been compared with a number of different unconstrained minimization techniques with indirect, direct, and random search methods [22]. It is concluded that the direct search methods using only function values are the best suited technique for the rotating machine design optimization. By using this proposed method, design optimization of a 3.7kW squirrel-cage IM with various objective functions, such as active material cost, annual energy consumption, total cost etc., is presented in [17]. The performance of GA and the Hooke-Jeeves method are compared in terms of performance and computation effort in design of an IM [23]. It is concluded that although the simulation time of the GA is a bit longer than that of the Hooke-Jeeves method, it converges better.

In [19], the multi-objective (light-weight and high efficiency) optimal design of IM for EV using a modified evolution strategy is presented. Total cost, manufacturing cost, power factor, starting torque, and break torque parameters are chosen as objective functions and the promising results have been achieved. In order to achieve the optimum IM design, an approach utilizing multi-objective (manufacturing cost, full load torque, and efficiency) fuzzy genetic algorithm (MFGA) is presented [21]. The proposed optimization method is compared with a single-objective genetic algorithm optimization method and it is concluded that MFGA is able to find more compromised solutions.

In [28], an optimization algorithm, which utilizes a sequential coupling of electromagnetic, thermal and fluid dynamics analyses is proposed in order to minimize the volume flow (to reduce the rated operation temperature). The optimization results show that it is possible to reduce the volume of conductor material and increase the efficiency at the same time. Apart from the design optimization, there are a number of studies on the optimization of efficiency and torque of IMs by designing an optimal controller/drive or optimizing the controller algorithm of the drive [25], [26].

In general, the design optimization involves more than one conflicting objectives, such as the material cost versus efficiency or high torque and high efficiency. However, it is not possible to optimize such objectives simultaneously. There are many other conflicting objectives such as the air-gap length versus torque ripple. A smaller air-gap can improve the torque and efficiency. However, it also causes the increase in torque ripple and acoustic noise. In the same manner, increasing the rotor slot opening leads to the decrease of torque ripple. However, it also causes a decrease in the average torque and output power. A machine with high torque necessitates lower efficiency or a high material weight and hence cost [18].

Apart from design optimization issue, performance improvement by changing some design parameters or slot shape is another critical and challenging topic that should be considered particularly for EV/HEV applications. In most cases, the performance can be improved up to a limited point with optimization. For further performance improvement, some geometric design parameters may be changed. Because of slotting and saturation effects, winding MMF and slip harmonics, the IMs contain high-order frequency components in the air-gap, particularly at the stator tooth tip parts and dominantly at the rotor tooth tip parts [27]–[31]. Because of substantial bar copper loss and subsequent overheating owing to air-gap flux density harmonics, the conventional rotor structure design with an open-slot cast rotor (OS) is not a good candidate for adoption in the EV/HEV applications [31]–[34]. A variety of alternative strategies have been proposed as follows in order to minimize the parasitic effects caused by the rotor part.

- Copper bars instead of aluminum bars [35], [36];
- Skewed rotor [37];
- Optimal rotor shape [30]–[32], [34], [38], [39];
- Stator, rotor slot number/pole number combination [28], [29], [40], [41];
- Unconventional control methods [42];
- Modulated rotor slots [43].

It has been demonstrated that using magnetic wedges can reduce the negative effects generated by open rotor slots, and as a result, enhance the IM's performance characteristics [44]. A skewed rotor is presented in [37] as an effective way to decrease stray loss and torque ripple. In addition, instead of using typical aluminum for the squirrel cage, copper is suggested to improve the efficiency and thermal properties [35], [36]. The great majority of studies in literature on rotor bar loss reduction are concerned with determining the best rotor slot shape for minimizing rotor bar losses. A closed

TABLE 1. Performance comparison of IMs having different nonoverlapping winding topologies.

Ref.	Slot/Pole (S/P) Combination	Topology	Fund. Winding Factor	MMF THD (%)	TpV* (kNm/m³)	PpV‡ (kW/m³)	Ease in assembling
[5]	24S/10P	3-layer FSCW with coils having different number of turns (ceiling fan stator)	0.861	45.06	4.73	1387.8	Very difficult
[6]	6S1/12S2/2P	4-layer FSCW with coils having different number of turns	0.36	20.63	10.01	3128.05	Difficult
[7]	30S/14P	2-layer FSCW with combined star-delta winding	0.64	38.72	35.37	19736.48	Very easy (similar to conventional FSCW)
[8]	24S/4P	Folded-strip toroidally wound winding	-	-	10.83	14174.4	Very difficult
[10]**	18S/6P	Advanced 2-layer FSCW	0.866	28.93	47.41	9359.48	Easy

*TpV: Torque per volume. ‡PpV: Power per volume. **Proposed topology.

rotor configuration with a u-shaped bridge is proposed in [34] to minimize the bar losses caused by air-gap flux density harmonics. Several various rotor slot configurations have been examined, and it has been determined that using a rotor with short bars is an effective approach for reducing losses of rotor bars due to harmonic fields in IMs [30]. It was hypothesized in [38] that by switching from a circular-bar design to a drop-shape bar design, the power density may be enhanced. An unconventional rotor configuration with un-even toot tips and narrower slot openings has been developed in [31] to simultaneously minimize time and space harmonics. Furthermore, many studies have focused on the best rotor slot design for improved torque and starting characteristics, such as line-start conditions, rotor bar losses, and evaluating alternative rotor slot designs [38], [39].

Torque ripple minimization approaches, unlike rotor bar loss reduction methods, have been thoroughly researched in terms of control [42] and design [40], [43] aspects. Modulated slot structures, consisting of asymmetric slot distributions, have been suggested in [43] to reduce synchronous torque and some parasitic effects such as noise, vibration, and undesired dips during the starting of IMs. In addition, many papers [28], [29], [40], [41] have emphasized the importance of stator slot, rotor slot, and pole number combinations on performance and parasitic effects. In addition, it has been demonstrated that the higher the rotor slot number, the lower the torque ripple, but the higher the rotor bar copper loss. Furthermore, solid-rotor structures are suggested for high-speed applications of inverted-fed IMs because of their robust constructions allowing working at much higher speeds. In addition, the solid-rotor IM has been demonstrated to have advantageous performance characteristics such as high-power density, high efficiency, high starting torque-to-starting current ratio, and high peak speed [45], [46].

The optimization of AIM is described in this paper using several optimization methodologies, including individual optimization, single-objective global optimization (SOGO), and multi-objective global optimization (MOGO). The Genetic Algorithm (GA) is utilized as an optimization tool, and the effectiveness of each optimization strategy is evaluated by comparing the optimal solutions. In addition, the methodology for determining and justifying optimization parameters will be detailed. Approach of closed rotor slot structures and influence of stack length with due account for the number of turns per phase will also be examined in order to further improve the power losses and FW characteristics. In addition, FEA was performed to evaluate the influences of various rotor slot designs on the SS and FW properties. The effectiveness of the optimization approach and the advantages of the proposed ANW topology have been revealed by designing globally optimized AIM and comparing some key performance characteristics over globally optimized CIM. Finally, in order to show the reliability of the FEA predictions performed in this study, the predicted (FEA) results of an CIM are experimentally verified.

II. ADVANCED NONOVERLAPPING WINDING (ANW) TOPOLOGY

Due to the restricted space available for traction machines in EV/HEV applications, reducing the end-winding length without compromising performance is critical. Despite the fact that the integer-slot distributed windings (ISDWs) have high winding factors and low space harmonics, resulting in minimal rotor power losses, they have long overhanging end-windings, resulting in a significant increase in overall axial length. One of the best methods to avoid overhanging end-windings in ISDWs is to switch from an overlapping to a nonoverlapping winding arrangement [5]–[9]. Therefore, an advanced winding topology with a nonoverlapping layout, whose basic schematic is depicted in Fig. 1, has been employed to achieve the aforementioned goal.

The lap-coil windings can be arranged with a variety of slot pitches using the proposed winding topology. This ANW topology, however, cannot be used for every stator slot/pole number (S/P) combination. There exist specific rules for suitable S/P combinations, as defined between (1) and (3).

$$n_t = y_c \quad \text{when } k_{wp} \neq 1 \tag{1}$$

$$\frac{S}{gcd\{S,P\}} = 3k \quad \text{when } k_{wp} \neq 1 \tag{2}$$

$$n_t = y_c - 1 \quad \text{if } k_{wp} = 1 \tag{3}$$

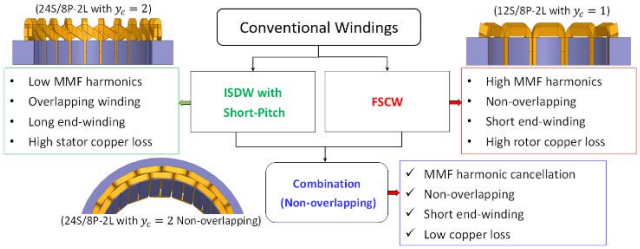

FIGURE 1. Schematic of ANW topology.

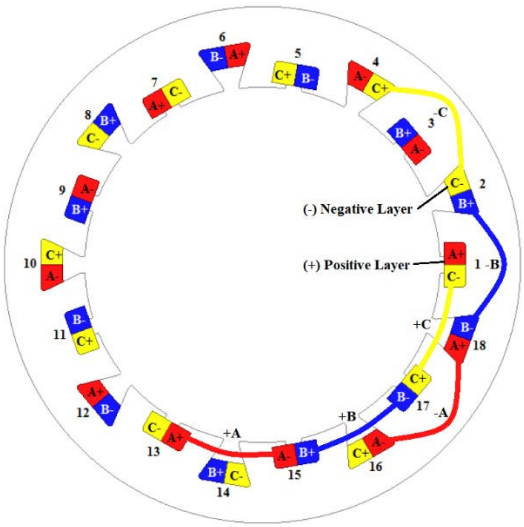

FIGURE 2. ANW layout of 18S/6P combination.

where y_c, n_t, k_{wp}, and k, are the coil pitch number, the overlay number, the fundamental winding factor, and a positive integer, respectively. (2) should be satisfied to use the lap-coils with multiple overlays where $gcd\{S, P\}$ denotes the greatest common divisor between P and S. For ANWs, n_t should be consistently equal to y_c and the fundamental winding factor harmonic must be different from unity. In addition, (3) is appropriate for combinations having unity fundamental winding factor. Conventional computation methods of winding factor and MMF are valid for ANWs. Winding arrangement for 18-stator slots/6-poles (18S/6P) combination, whose fundamental winding factor is 0.866, is created as an example and shown in Fig. 2. More details about the ANW topology and winding analysis can be found in [11].

III. DESIGN OPTIMIZATION OF AIMs

As explained in the Introduction section, the GA technique has proved to be an effective tool for electrical machine design optimization. Because, as evidenced from literature [47]–[51], it can solve multi-objective problems more accurately, and it does not require any experimental data to perform. In addition, one of the most significant benefits of the GA over evolutionary algorithms is that it can identify the global minimum rather than a local minimum, and that the initial efforts with various starting points do not have to be near to real values [47], [48]. Another benefit of GA method is that it does not necessitate the usage of the function's derivative, which is not always readily available or may even exist. However, as reported in [49], GA technique requires the objective function to be evaluated several times and thus require high computational effort and time. Nevertheless, as will be shown in the following sections, prior to the optimization by GA, performing an individual optimization provides a good initial guess and starting point by determining the most important parameters and their constraints. Therefore, the global optimum can be reached more quickly and accurately.

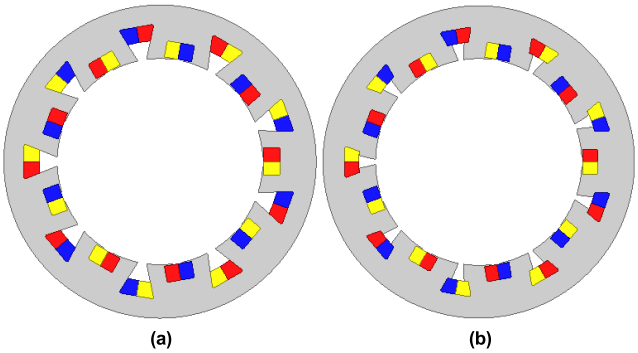

FIGURE 3. Feasible stator structures for ANW topology. (a) Straight slot structure. (b) Zig-zag slot structure.

A. DETERMINATION OF DESIGN PARAMETERS

Individual and global optimization methodologies can be used to optimize the IMs. Alternatively, it is practical to determine the optimal geometrical parameters using an individual optimization approach, which implies that an individual optimization is necessary for each geometric parameter. Following that, utilizing GA, individually optimized numerous geometry parameters can be optimized using the global optimization approach. Conducting an individual optimization is highly beneficial at the beginning when determining the precise constraints of the global optimization. In addition, employing individual optimization prior to the GA helps reach the global optimal more quickly. An individual optimization strategy can also be used to validate the effectiveness of the global optimization approach. One of the most significant factors to consider is that because the systematic and logical are crucial in the individual optimization technique, the design parameters should be ordered according to their sensitivity [52].

The feasibility of stator constructions for ANWs has also been investigated in this study. As a result of the NW topology, some of the stator slots cannot be completely filled, as seen in Fig. 3(a). In order to minimize the saturation level of the stator teeth, these vacant spaces might be filled with extra iron core material. As a result, utilizing a zig-zag slot arrangement, as shown in Fig. 3(b), can result in reduced magnetic saturation in stator teeth.

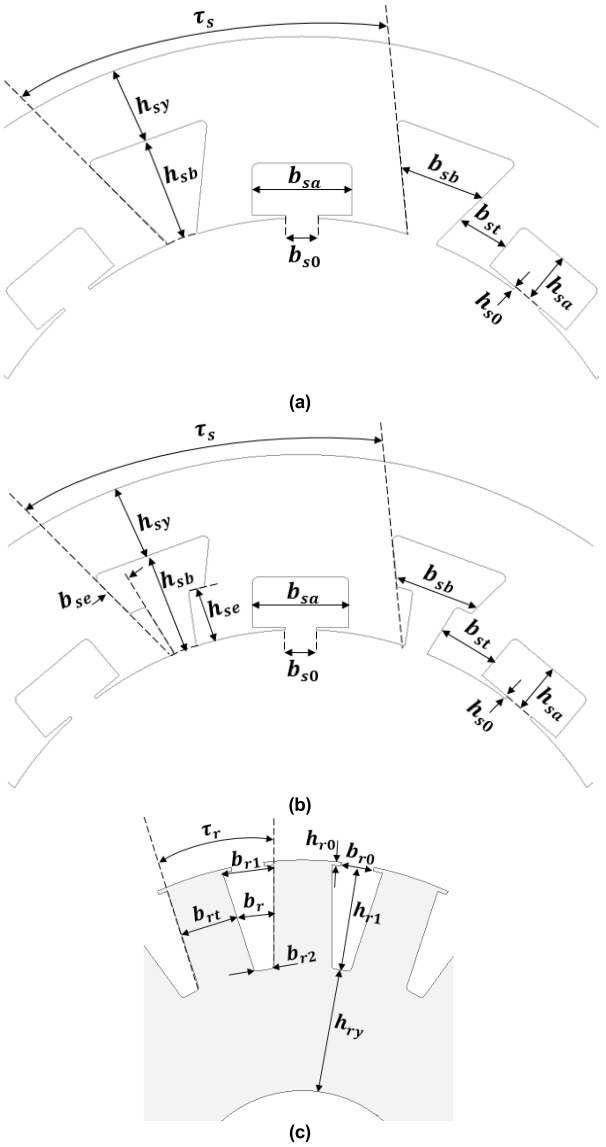

FIGURE 4. Geometric design variables of the AIM. (a) Straight stator slot structure. (b) Zig-zag stator slot structure. (c) Rotor structure.

Fig. 4 depicts the design parameters that will be optimized in this work. As can be observed, compared to the straight slot, the zig-zag slot has two additional parameters, namely width (b_{se}) and height (h_{se}) and the identical rotor (see Fig. 4(c)) is employed during the optimization process. Note that only the optimization of geometric design parameters has been considered in this study. Apart from these parameters, parametric determination of other key specifications such as stack length, number of turns, air-gap length, slot numbers, etc. is presented in [11].

The initial design parameters for 3-phase AIMs with straight and zig-zag slot topologies are listed in Table 2. Note that the lamination material is M270 with stacking factor of 0.92 and 0.35mm lamination thickness. In addition, both the bar and end-ring materials are Copper 75°C. The major design specifications of the globally optimized CIM have also been listed in Table 1 to show that a fair comparison has been made by designing AIM and CIM with the same major specifications such as outer diameter, stack length, and pole number, etc. Table 3 lists the definitions and individual optimization sequences for the design parameters. Although the slip is not a genuine optimization parameter, the slip at the pull-out torque must be determined before each parameter is individually optimized.

The determination of excitation is another criterion that should be addressed throughout the optimization procedure.

TABLE 2. Initial major design parameters*.

Parameter	AIM	CIM[‡]	Parameter	AIM	CIM[‡]
$S/R/P$	18/20/6	54/44/6	b_{st}	7.34	3.85
ℓ	70	70	b_{se}	3.1	-
D_{so}	144	144	h_{se2}	6.12	-
D_{si}	98.8	104.112	g	0.35	0.35
N_t	12	9	a	6	2
h_{sy}	9.28	8.92	D_{ri}	30	30
h_{s0}	0.65	0.5	h_{r0}	0.6	0.5
h_{sa}	6.56	-	h_{r1}	14	12.6
$h_{sb} = 2h_{sa}$	13.12	-	h_{ry}	18.5	23.65
b_{s0}	4.5	2	b_{r0}	3.5	2
b_{sa}	14.28	-	b_r	4.25	2.68
b_{sb}	10.5	-	b_{rt}	8.63	3.75

*All dimensions are in mm; D_{so}: Outer diameter of stator; D_{si}: Inner diameter of stator; ℓ: Active stack length, g: Air-gap length; a: Number of parallel branches; D_{ri}: Shaft diameter. [‡]For CIM: all given parameters have been globally optimized.

TABLE 3. Definitions of stator and rotor geometric parameters according to order of sensitivity.

#	*Explanation*	*Equation*
–	Slip	$s = 100 \cdot \left(1 - \frac{n_s}{n_r}\right)$
1	Stator split ratio	$\lambda_s = \frac{D_{si}}{D_{so}}$
2(*a*)	Stator slot width ratio	$b_s = 1 - \frac{2b_{st}}{\tau_s} = \frac{b_{sa} + b_{sb}}{\tau_s}$
2(*b*)	Stator slot width ratio for zig-zag stator structure	$b_{ser} = 1 - \frac{2b_{se}}{b_{sb}}$
3(*a*)	Stator yoke thickness ratio	$h_s = \frac{h_{sy}}{h_{sy} + h_{sb}} = \frac{h_{sy}}{h_{sy} + 2(h_{sa} + h_{s0})}$
3(*b*)	Stator yoke thickness ratio for zig-zag stator structure	$h_{ser} = \frac{h_{se}}{h_{sb}}$
4	Rotor slot width ratio	$b_{rr} = \frac{b_r}{\tau_r}$
5	Rotor yoke thickness ratio	$h_r = \frac{h_{ry}}{h_{ry} + h_{r1} + h_{r0}}$
6	Stator slot opening ratio	$b_{sor} = \frac{2b_{s0}}{\tau_{sb}}$
7	Rotor slot opening ratio	$b_{ror} = \frac{b_{r0}}{b_r}$

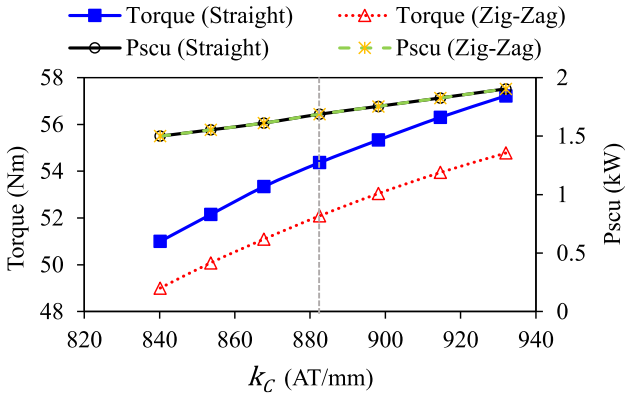

FIGURE 5. Average torque and stator copper loss against stator copper loss coefficient.

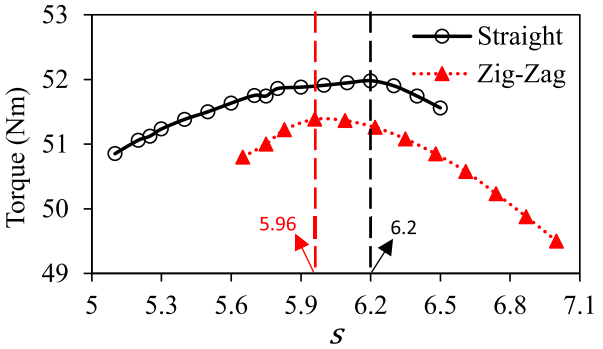

FIGURE 6. Average torque against slip percentage.

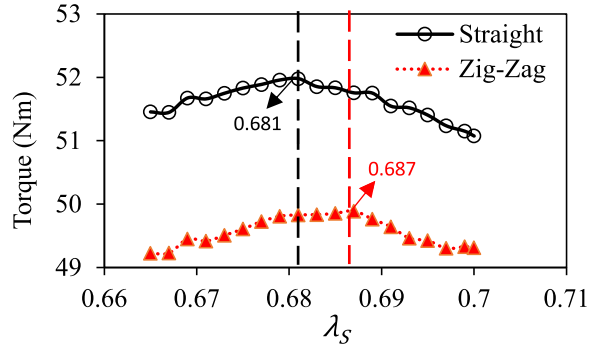

FIGURE 7. Average torque versus split ratio.

The phase current, stator current density, or stator copper loss could be chosen as excitation source. The excitation source used in this study is chosen as fixed stator copper loss. The stator copper loss can be calculated by (4),

$$P_{scu} = 3\frac{I_s^2}{a^2}R_{phase} = \frac{6J_s^2N_t^2}{a^2k_f}N_cA_s\rho_{cu}\left[\ell + \tau_s - \left(\frac{b_{sa}+b_{sb}}{4}\right)\right] \quad (4)$$

$$I_s = \frac{k_c\sqrt{A_s}}{Nt} \quad (5)$$

$$k_c = J_s\sqrt{A_s} = \frac{I_sN_t}{\sqrt{A_s}} = \frac{I_sN_t}{\sqrt{b_{sa}h_{sa}}} \quad (6)$$

$$P_{scu} = 3\frac{I_s^2}{a^2}R_{phase} = \frac{6k_c^2N_t^2}{a^2k_f}N_c\rho_{cu}\left[\ell + \tau_s - \left(\frac{b_{sa}+b_{sb}}{4}\right)\right] \quad (7)$$

where I_s, R_{phase}, J_s, N_t, a, k_f, N_c, A_s, ρ_{cu}, k_c, and ℓ represent the phase current, the phase resistance, the stator current density, the number of turns per the coil, the parallel branch number, the slot fill factor, the number of coils, the stator slot area, the resistivity of the copper, and the active stack length, respectively. The current is assessed using k_c as described in (5) [52] to maintain the stator copper loss constant during individual optimization. In fact, the torque generation under a fixed copper loss scenario requires this coefficient, which is derived by (6). As a result, the torque and copper loss are proportional to this coefficient, as given in (7).

B. INDIVIDUAL PARAMETER OPTIMIZATION

By using the expressions from (4) to (7), the variations of average torque and stator copper loss are illustrated in Fig. 5. During the individual optimization, the copper loss of 1.7kW@80°C, which is equivalent to $k_c \cong 880$, is assumed with a slot fill factor of 0.6, i.e. $k_f = 0.6$.

The pull-out torque slip values for straight and zig-zag slot topologies are 6.2 and 5.96, respectively, as shown in Fig. 6. To obtain optimal values as rapidly as feasible, the number of optimization parameters should be kept to a minimum. Thus, it is very useful to use ratios for interdependent parameters. Consequently, selecting the parameters that have the most impact on the optimization objectives, such as time-averaged torque, power losses, torque ripple, etc., is of great importance. Under these circumstances, the design parameters are optimized in the following order as listed in Table 3:

1. stator split ratio;
2. stator slot width ratio;
3. stator yoke thickness ratio;
4. rotor slot width ratio;
5. rotor yoke thickness ratio;
6. stator slot opening ratio;
7. rotor slot opening ratio.

The variations of the time-average torque with respect to split ratio, stator slot width ratio, and stator yoke thickness ratio for both of the straight and zig-zag slot are illustrated between Fig. 7 and Fig. 9. Individually optimized values are chosen for the parameters that yield the highest torque during pull-out slip. It is also obvious that the AIM with straight slot structure has a far greater average torque than that of the AIM with zig-zag slot structure. Investigating the figures from Fig. 10 to Fig. 12 can reveal the underlying cause.

Fig. 10 reveals that there is a linear correlation between the stator slot width ratio b_{ser} and torque while there exists an inverse correlation between stator slot height ratio h_{se} and

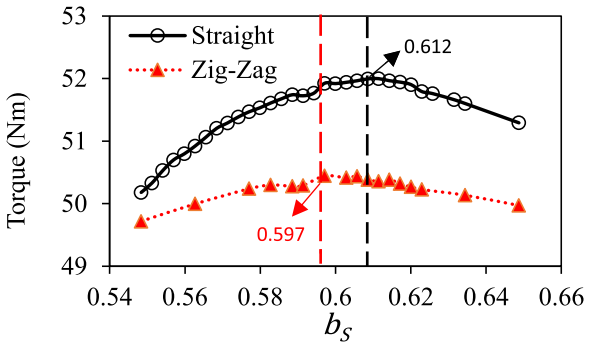

FIGURE 8. Average torque against stator slot width ratio.

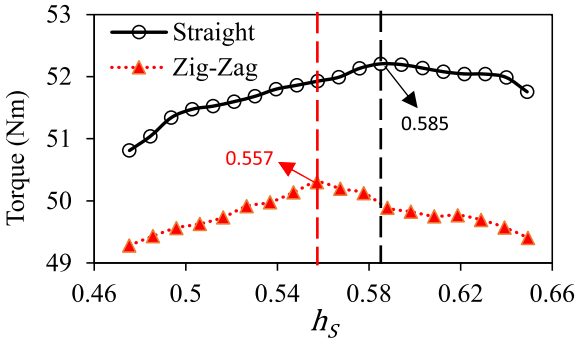

FIGURE 9. Average torque versus stator yoke thickness ratio.

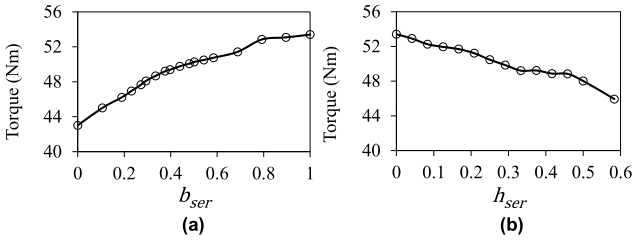

FIGURE 10. Variation of average torque. (a) With stator slot width ratio. (b) With stator yoke thickness ratio of zig-zag slot structure.

torque. In fact, once b_{ser} is equal to unity or accordingly h_{ser} is equal to zero, the structure of the zig-zag slot transforms into the straight slot structure as seen in Fig. 11. Considering Fig. 10 and Fig. 11, it can be concluded that the zig-zag slot structure causes a substantial increase in amplitudes of short-circuited and leakage-flux. It is possible to observe the same phenomenon from Fig. 12. Note that the leakage component of the slot flux density is the tangential component, whereas the torque generation component is the radial component, as discussed in [53]. As a result of these observations, it can be concluded that the zig-zag slot structure is not electromagnetically feasible for the AIMs. Therefore, since zig-zag slot design sacrifices torque greatly, only the optimization of AIM with a straight slot structure will be addressed in the following sections.

Fig. 13 and Fig. 14 show the results of individual optimization of the rotor slot parameters. Apart from the ratios providing the highest torque, there are different optimum ratios ensuring the minimum torque ripple. However, because

TABLE 4. Comparison between initial and individual optimized variables.

#	Parameters	Initial value	Individual Optimized
-	s	5.75	6.2
1	λ_s	0.686	0.681
2	b_s	0.628	0.612
3	h_s	0.56	0.585
4	b_r	0.371	0.352
5	h_r	0.46	0.483
6	b_{sor}	0.37	0.385
7	b_{ror}	0.3	0.28

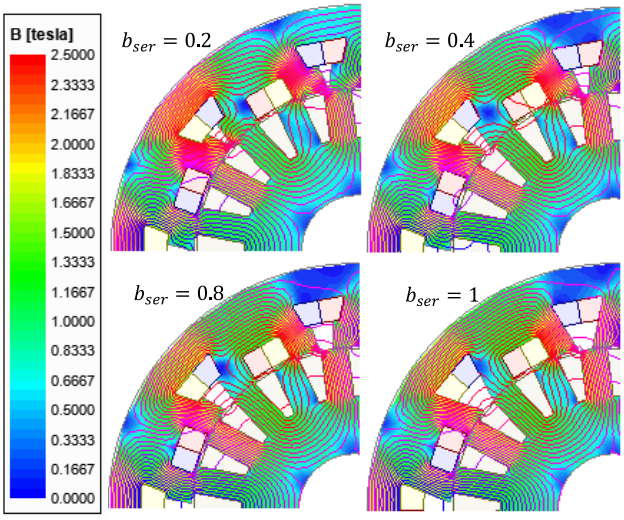

FIGURE 11. Flux density and flux line distributions of zig-zag slot AIM with numerous stator slot width ratios.

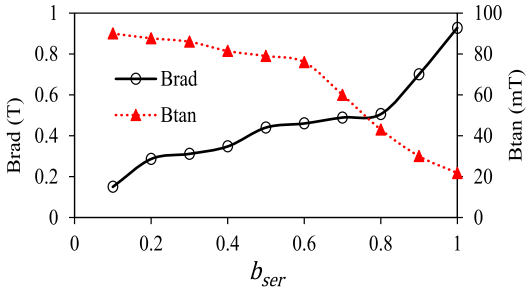

FIGURE 12. Radial and tangential components of the stator slot flux density of the AIM with zig-zag slot structure.

the objective in this section is to optimize the average torque, the ratios that provide maximum torque have been chosen as the optimal values. Although the cross-coupling effect of the parameters have not been considered in the individual optimization, a ∼5% higher average torque is achieved compared to initial design. h_{s0} and h_{r0} parameters were not optimized in this work since their impact on performance is insignificant or negative [54]. As a result, they have been set to their mechanically allowable limits.

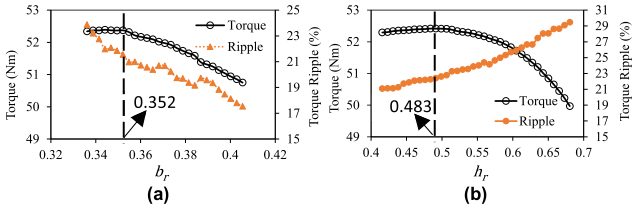

FIGURE 13. Variation of torque and torque ripple. (a) With b_r. (b) With h_r.

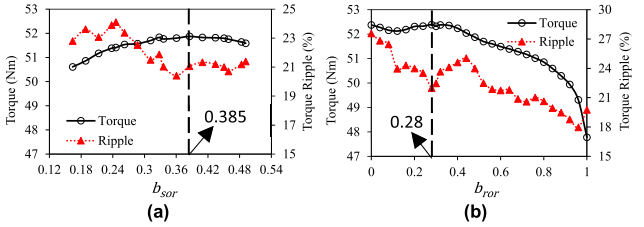

FIGURE 14. Variation of torque and torque ripple. (a) With b_{sor}. (b) With b_{ror}.

Table 4 lists the initial and individually optimized values of the optimization parameters. It has been deduced that wider stator slot tooth and opening widths, smaller and shallower rotor slot, narrower rotor slot opening width and thinner yoke thickness are preferable to provide greater torque for the given parameters as compared to the initial design.

C. SINGLE-OBJECTIVE GLOBAL OPTIMIZATION

The Genetic Algorithm (GA), which is one of the most successful numerical optimization tools, has been widely employed to investigate the optimal IM solutions. The GA is a random search process for optimization analysis that searches the solution space using mechanisms that provides natural selection, such as subsequent generations and mutations. In each generation, some new members ''children'' are generated, and the mature population engages in a natural-selection process that consecutively decreases the population size to a desirable level ''next generation.''

In this section, due to the major effect of the objective function on the optimization outcomes, the global optimization of AIM is performed with two different restrictions: maximum current density and maximum stator copper loss. The following are the parameters for single-objective global optimization (SOGO): The parent size (population size), mating pool size, children size, Pareto Front size (number of survivors), next generation population size, roulette selection, crossover probability, and mutation probability size are 30, 30, 30, 10, 30, 10, 1, and 2, respectively. In addition, the maximum generation (iteration) number is selected as 1000. The single objective is to maximize the time-averaged torque of the AIM to its feasibly available value at the SS operating region. For single-objective optimizations, the cost functions are adopted as the sum of absolute weighted values w_i of the individual goal errors e_i at a certain slip value, as described in (8).

$$Cost = -\sum_{i=1}^{N} w_i e_i \tag{8}$$

TABLE 5. Global optimization variables with R1 and R2 restrictions.

Par.	Init. Val.	Ind. Opt.	Constraints for J_s Rest.	GO R1	Constraints for P_{scu} Rest.	GO R2
λ_s	0.686	0.681	[0.66:0.71]	0.687	[0.65:0.69]	0.689
b_s	0.628	0.612	[0.58:0.64]	0.618	[0.585:0.65]	0.616
h_s	0.56	0.585	[0.48:0.6]	0.58	[0.48:0.6]	0.585
b_r	0.371	0.352	[0.3:0.4]	0.362	[0.2:0.41]	0.344
h_r	0.46	0.483	[0.35:0.5]	0.473	[0.285:0.544]	0.418
b_{sor}	0.37	0.385	[0.3:0.45]	0.39	[0.3:0.45]	0.389
b_{ror}	0.3	0.28	[0.1:0.4]	0.27	[0.083:0.423]	0.281

1) OPTIMIZATION WITH RESTRICTION OF MAXIMUM CURRENT DENSITY (R1)

For IMs with liquid cooling in ducts, the typical permitted continuous current densities are 23 to 31A/mm^2 [53]. As a result, for the maximum current density of $J_s = 31$A/mm^2, the copper loss coefficient k_c is assigned as ∼883. The single-objective optimization process for the maximum current density is shown in Fig. 18.(a), and the solutions are presented in Table 5, together with the individual optimization results.

2) OPTIMIZATION WITH RESTRICTION OF MAXIMUM STATOR COPPER LOSS (R2)

With 0.6 stator slot fill factor and $k_c = 883$, the stator copper loss is limited to 6.1kW. Fig. 15(b) depicts the single-objective optimization procedure for the specified stator copper loss. Table 4 also contains the solutions to the optimized parameters as well as the individual optimization results.

3) SOGO PROCEDURE BY GA

In Fig. 15, the computed cost against iteration is shown, together with the local optimum points for both the maximum current density and maximum copper loss density limitations. It can be observed that the cost is large at the start of the optimization and gradually decreases as the number of iterations increases. However, it is also recognized that the GA has leaped out of the local optimum points due to its random nature. Even though the same number of variables were altered during the optimization methods, the ideal torque was attained in much less time in case of the maximum current density restriction. In terms of cost, the optimal torque achieved from the optimization with the restriction of the maximum current density is slightly higher than that of the optimization with the maximum stator copper loss. Table 5 lists the obtained solutions and the optimal values.

D. MULTI-OBJECTIVE GLOBAL OPTIMIZATION

IM design optimization is finding a balance between conflicting objectives such as high average torque, high power factor, high efficiency, small size, low cost, etc. Because there are so many competing optimization objectives, multi-objective optimization techniques are necessary to achieve the design objectives. The objective functions in multi-objective opti-

mization produce a multi-dimensional space in addition to the natural selection variable space, which is one of the key distinctions between single-objective and multi-objective optimization.

In this part, the time-averaged torque, stator copper loss and rotor bar copper loss have been chosen as objectives to be optimized. Because the objective function has such a major effect on the optimization outcomes, AIM's MOGO is done with and without rotor bar current density restrictions. The same GA settings as the SOGO is employed for the MOGO to optimize the desired objectives.

1) JUSTIFICATION OF OBJECTIVES AND GOALS

The most attractive objectives for a given outer diameter and stack length are to maximize the practically available torque and efficiency or reduce the prevailing machine losses. The total copper losses, which include the stator windings, and rotor bars, and end-rings, are the most significant loss partition of an IM in the constant torque operating region. In this study, it is intended to optimize the AIMs at the constant torque operating region (at relatively low-speed and hence low frequency). The core loss partition is small in comparison to the overall copper loss because the frequency is low in this region.

Another essential factor to consider is the amount of time spent. When the IM is considered, achieving the SS result from any simulation takes a substantial time compared to synchronous machines as a consequence of inducing voltages of many different frequencies in the rotor bars. Thus, it can be predicted that with fewer optimization variables and also objectives, the optimal solution may be reached more rapidly. Therefore, the same objectives, which are the time-averaged torque, stator copper loss, and rotor bar copper loss are chosen for both the optimizations with and without the restriction of the rotor bar current density.

2) JUSTIFICATION OF OBJECTIVES AND WEIGHTS

Special attention should be made while explaining the objectives and their weights in order to reach the optimization solution more rapidly. The objectives are justified as follows, considering the previously acquired individual and global optimization solutions, as well as calculated copper losses. The maximum torque that may be obtained for specified machine volume is calculated as ∼54Nm by using the torque equation given in (10) derived from (9),

$$S_{out} = 11 k_w B_g a_c D_{so}^2 \ell n_r \tag{9}$$

$$P_{out} = T\omega \rightarrow T = \frac{S_{out} cos\,\varphi}{\frac{2\pi n_r}{60}} = \frac{330}{\pi} D_{so}^2 \ell a_c k_{wp} B_g cos\,\varphi \tag{10}$$

where S_{out}, T, ω, P_{out}, D_{so}, a_c, n_r, B_g, and $cos\,\varphi$ are the apparent power, the electromagnetic torque, the angular speed, the active power, the stator outer diameter, the electric loading, the rotor speed, the average air-gap flux density, and the power factor, respectively. Considering the current density, efficiency, and the average torque of initial design at 500A (rms), the torque objective is justified as being 54.5Nm as given in Table 5. Only the stator slot copper losses may be computed during the optimization since the optimization was carried out using the 2-D FEA. Consequently, for both optimization options, the stator slot copper loss $P_{scu(MOGO12)}$ is justified by using (11),

$$\begin{aligned} P_{scu(SOGO-R1)} &< P_{scu(MOGO12)} < P_{scu(SOGO-R2)} \\ &\rightarrow P_{scu(MOGO12)} \\ &\approx \frac{P_{scu(SOGO-R1)} + P_{scu(SOGO-R2)}}{2} \end{aligned} \tag{11}$$

where $P_{scu(SOGO-R1)}$ and $P_{scu(SOGO-R2)}$ are the stator slot copper loss obtained from the SOGO solution in case of maximum stator current density restriction and in case of maximum stator copper loss restriction, respectively. In the same method, the time-averaged rotor copper losses with/without the restriction of rotor bar current density are justified by considering (12) and (13).

$$\begin{aligned} P_{rcu(Max\_S_{bar})} &< P_{rcu(MOGO1)} < P_{rcu(Min\_S_{bar})} \\ &\rightarrow P_{rcu(MOGO1)} \\ &\approx \frac{P_{rcu(Max\_S_{bar})} + P_{rcu(Min\_S_{bar})}}{2} \end{aligned} \tag{12}$$

$$\begin{aligned} P_{rcu(Min\_Cost)} &< P_{rcu(MOGO2)} < P_{rcu(Max\_Cost)} \\ &\rightarrow P_{rcu(MOGO2)} \\ &\approx \frac{P_{rcu(Min\_Cost)} + P_{rcu(Max\_Cost)}}{2} \end{aligned} \tag{13}$$

In (12), $P_{rcu(Max\_S_{bar})}$ and $P_{rcu(Min\_S_{bar})}$ designate the maximum and minimum rotor bar losses obtained in cases of maximum and minimum rotor bar surface areas, correspondingly. In (13), $P_{rcu(Max\_Cost)}$ and $P_{rcu(Min\_Cost)}$ specify the rotor bar copper losses in cases of the maximum cost and minimum cost attained from the SOGO-R2, respectively. Therefore, after the assessment of the justified objectives, their weights, showing the importance of the objective, are also designed and listed together with the objectives in Table 6.

Both torque and efficiency are critical factors in EV/HEV applications, and they should be as high as feasible during any driving cycle. When getting the highest torque and efficiency at the same time is not attainable, high torque is favoured over high efficiency in some scenarios. As a result, in both optimizations, the weight of the torque is assigned to be somewhat greater.

3) COST FUNCTION FOR MOGO

The weighted total of the sub-goal errors is used to calculate the cost function. The divergence between the simulated reaction and the goal value restriction is represented by an error value for each sub-goal. The cost value becomes 0 if the simulation response meets the objective limit. Alternatively, the difference between the simulated response and the given objective constraint defines the error value. Thus, the cost

TABLE 6. Justified objectives and their weights.

	With J_r restriction		Without J_r restriction	
Variable	Condition	Weight	Condition	Weight
Average torque (Nm)	≥ 54.5	0.41	≥ 54.5	0.41
Average stator slot copper loss (kW)	≤ 1.35	0.26	≤ 1.35	0.29
Average rotor copper loss (kW)	≤ 0.85	0.32	≤ 1	0.30

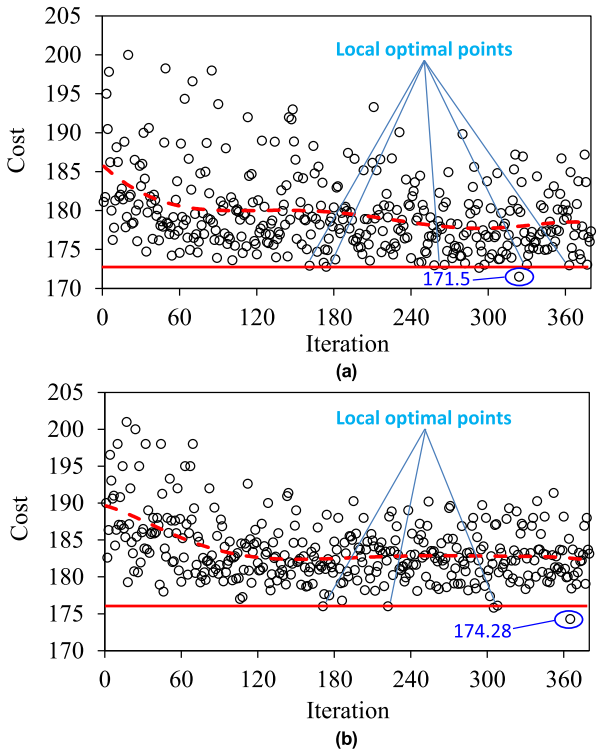

FIGURE 15. Optimization produced by single-objective GA. (a) With restriction of maximum current density (SOGO-R1). (b) With restriction of maximum stator copper loss (SOGO-R2).

function is described as expressed in (14),

$$Cost = \sum_{j=1}^{G} \frac{w_j}{N_j} \sum_{i=1}^{N_j} e_{ji} \tag{14}$$

where G, w_j, N_j, e_{ji} are the sub-goal number, the weight factor related with the j^{th} sub-goal, the number of frequencies for the j^{th} sub-goal, and the error contribution from the j^{th} sub-goal at the i^{th} frequency, respectively. Here, the value of e_i is determined by the band conditions, target value, and the simulated response value.

4) MOGO PROCEDURE BY GA

The optimal solutions with and without the bar current density restrictions are found as shown in Fig. 16. It can be observed that in comparison to SOGO, longer time was consumed to achieve the global optimum solutions. Table 7 lists the established constraints and the optimal values of design parameters.

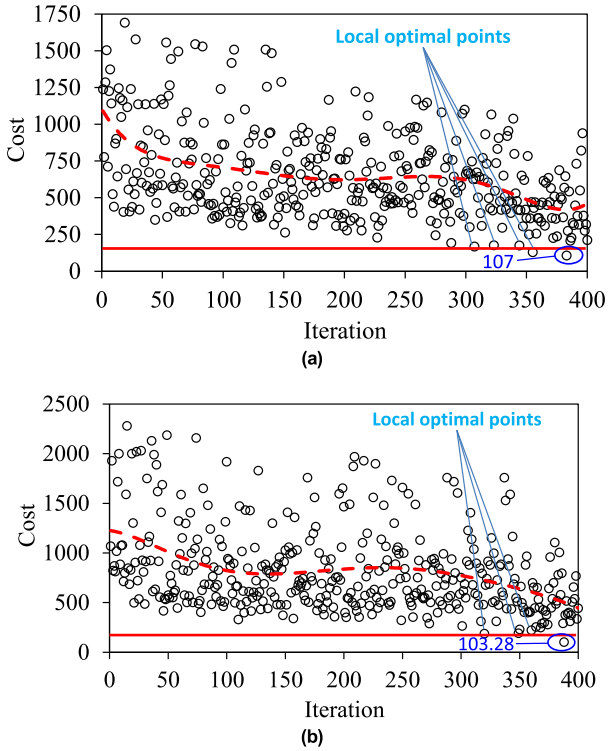

FIGURE 16. Optimization produced by multi-objective GA. (a) With restriction of maximum current density (MOGO-R1). (b) With restriction of maximum stator copper loss (MOGO-R2).

TABLE 7. Comparison between initial and individual optimized values.

Par.	Init. Val.	Ind. Opt.	Constraints for J_r Rest.	GO R1	Constraints without J_r Rest.	GO R2
λ_s	0.686	0.681	[0.65:0.7]	0.695	[0.655:0.698]	0.708
b_s	0.628	0.612	[0.604:0.646]	0.605	[0.65:0.683]	0.595
h_s	0.56	0.585	[0.526:0.611]	0.549	[0.48:0.588]	0.525
b_r	0.371	0.352	[0.3:0.427]	0.362	[0.134:0.47]	0.329
h_r	0.46	0.483	[0.42:0.5]	0.498	[0.279:0.592]	0.388
b_{sor}	0.37	0.385	[0.3:0.47]	0.45	[0.3:0.469]	0.436
b_{ror}	0.3	0.28	[0.36:0.5]	0.243	[0.249:0.554]	0.276

IV. PERFORMANCE COMPARISON OF OPTIMIZED AIMs

A. DESIGN COMPARISON

In order to reveal the effectiveness of the proposed optimization method and also the proposed winding topology, the obtained optimization results have been compared with globally optimized conventional IM (CIM) having 54S/44R/6P combination, 9 coil-pitches double-layer ISDWs and the same operating and geometric design specifications with AIMs (see Table 1). The 2-D views of CIM and AIMs optimized with SOGO and MOGO methods are shown in Fig. 17 and Fig. 18 respectively.

Although the S/R/P combination, outer diameter and the stack lengths remain constant, the geometries of the stator and rotor slots alter based on the constraints, restrictions and optimization method. The machine weights and the costs are

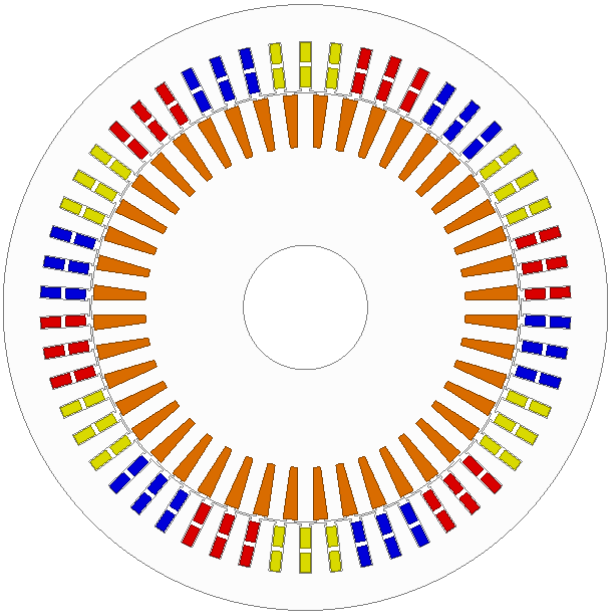

FIGURE 17. 2-D view of globally optimized CIM.

evaluated by using (15),

$$M_{Tot} = D_{W270}\left(A_{score} + A_{rcore}\right)\ell + 2D_{cus}N_cA_{scoil} \cdot \left[\ell + \tau_s - \left(\frac{b_{sa}b_{sb}}{4}\right)\right] + D_{cur}\left(RA_{Bar}\ell + 2A_{Ring}\ell_{Ring}\right) \quad (15)$$

where D_{W270}, A_{Score}, A_{Rcore}, D_{Cu_S}, D_{Cu_R}, N_c, $A_{S_{coil}}$, R, A_{Bar}, A_{Ring}, ℓ_{Ring} are the mass density of core material, the stator area, the rotor area, the mass density of stator windings, the mass density of rotor bars, the total number of coils, the stator slot area with fill factor, the rotor slot number, the area of the bar and ring copper, and the axial length of the one ring piece, respectively. The materials' costs are calculated by using data given in Table 8. Note that the current material prices are obtained from London Metal Exchange (LME) database [55]. The calculated mass and the total cost are compared in Table 9. As seen, although there exists no significant difference between the masses of AIMs, the candidates requiring more copper are more expensive than others because of the ∼21 times higher cost of the copper material compared to core material. Because of the same reason, the total cost of the CIM is more expensive than those of AIMs. In addition, compared to initial design's total cost, the total costs of the optimized AIMs have been reduced considerably. The cheapest AIM is accomplished since the stator copper usage is reduced (see Table 10(f)). Without changing the number of turns, the copper usage is decreased by reducing the diameter of wire. In this case, however, the current density increases since the phase current remains constant, and hence more cooling equipment, causing an increase in the cost, may be required.

TABLE 8. Active material mass density and cost.

	Mass Density (kg/m^3)	Cost ($/kg)
Copper (Stranded)	8933	9.835
Copper (Solid Bar)	8960	9.835
Steel (W270_35)	7650	0.47

TABLE 9. Design comparison table.

		Core Mass (kg)		Copper Mass (kg)		Total Mass (kg)	Total cost ($)
	Design	S	R	S	R		
	CIM	3.39	2.92	1.73	1.32	9.36	32.94
(a)	Initial	3.47	2.95	1.07	1.16	8.65	24.95
(b)	Ind. Opt.	3.75	2.95	1.1	1.06	8.86	24.34
(c)	SOGO with J_s Rest.	4.07	2.81	0.88	0.93	8.69	21.04
(d)	SOGO with P_{scu} Rest.	3.99	2.81	0.96	0.93	8.69	21.8
(e)	MOGO with J_r Rest.	3.46	2.92	1.01	1.25	8.64	25.18
(f)	MOGO without J_r Rest.	3.97	2.98	0.8	0.95	8.7	20.49

S: Stator; R: Rotor.

B. PERFORMANCE COMPARISON

Some major electromagnetic performance characteristics, acquired from optimized CIM and AIMs, are compared in this section. The electromagnetic performance parameters are evaluated using 2-D FEA in SS with a synchronous speed of 2000rpm and a rated stator current of 500Arms. Compared to the initial design (a), the highest average torque, obtained by SOGO with stator current density limitation (c), is improved by 12.8% thanks to the global optimization by using genetic algorithm. Although candidates have high torque ripple, it can be decreased by changing the rotor slot opening shape parameters, as will be shown in the next section.

Table 10 summarizes major electromagnetic properties of the initial and optimized AIMs to demonstrate the effectiveness of the optimization approaches and identify the best suitable candidate. In addition, the performances of globally optimized AIM candidates have also been compared to CIM to reveal the advantages of the proposed NSW topology. Higher torque, higher efficiency, low weight, and minimal space requirements are the most demanding criteria in EV/HEV applications.

In addition, the thermal properties should be considered while determining the size of the cooling equipment. Consequently, considering the size of the cooling equipment, the current density levels should be as low as feasible to preserve as much room as possible in the vehicle. It has been found that although the individual optimization method is not as good as global optimizations, it is a superb tool for determining initial parameters, precise limitations, and the criteria or boundaries of the objectives. In addition, if the variable constraints and objective conditions are precisely established using the individual optimization approach, the optimal solution may be achieved using the SOGO without the need of the MOGO. Considering the time-consuming

TABLE 10. General comparison of the optimization results.

	CIM	(a)	(b)	(c)	(d)	(e)	(f)
T (Nm)	52.21	50.4	52.22	56.85	56.435	54.052	54.725
ΔT (%)	4	21.83	27.003	18.11	19.7	18.44	18.67
s (%)	4.75	6.2	5.335	6.2	6.536	5.75	4.483
P_{out} (kW)	10.415	10.21	11.476	12.775	12.646	10.67	12.523
η (%)	75.343	74.236	73.962	75.57	75.5	75.884	76.15
ℓ_a (mm)	122	80.4	81.85	79.5	80.2	80.25	75.77
M_T(kg)	9.36	8.65	8.86	8.69	8.69	8.64	8.7
Cost ($)	32.94	24.95	24.34	21.04	21.8	25.18	20.49
J_s (A/mm^2)	22.32	29.17	29.88	31	29.87	30.96	31
J_r (A/mm^2)	13.54	17.862	20.222	27.833	28.772	17.51	19.29

T: average torque, ΔT: torque ripple, s: slip, P_{out}: output power, η: efficiency, ℓ_a: total axial length, M_T: total mass, J_s: stator current density, J_r: rotor current density.

nature of IM analysis (reaching transient state takes a relatively long time), the fastness of optimization algorithm is great of importance. It is also demonstrated that with specific constraints, such as stator copper loss, rotor bar current density, and so on, the optimal solution may be found more rapidly.

The comparison of the major electromagnetic performance characteristics has been summarized as follows:

- Thanks to the short end-winding lengths of ANW topology, ∼34% shorter initial design (a) having comparable torque and efficiency with the CIM is achieved. However, after MOGO, AIM candidates having higher torque and efficiency than those of CIM are obtained.
- Although candidate (c) has the highest torque and output power, candidate (f) has the highest efficiency;
- Torque ripple of candidate (c) is the minimum;
- Although candidate (f) has the shortest axial length and total mass and hence cost, the initial design has the minimum current density;
- Although candidate (f) is the most compact and cheapest one, it requires more cooling equipment due to the higher stator and rotor current densities. However, simultaneous parametric analysis or global optimization of the number of turns and stack length may result in further improved performance.

As a result, if the size is the most important criteria, then the most favourable candidate is (f). If electromagnetic performance is the most significant criterion, on the other hand, the best choice is (c). In terms of overall characteristics including thermal properties, (e) is the best choice.

V. PERFORMANCE IMPROVEMENT METHODS

Apart from compactness, smooth drive (low torque ripple) and high-torque at high-speed are also required features in EV/HEV applications. In the previous sections, global optimization of the AIMs has been presented. In this section, further SS and FW performance improvements of AIMs will be presented. In addition, the effectiveness of ANWs and performance improvement methods will be evaluated over AIM's globally optimized conventional (CIM) counterpart.

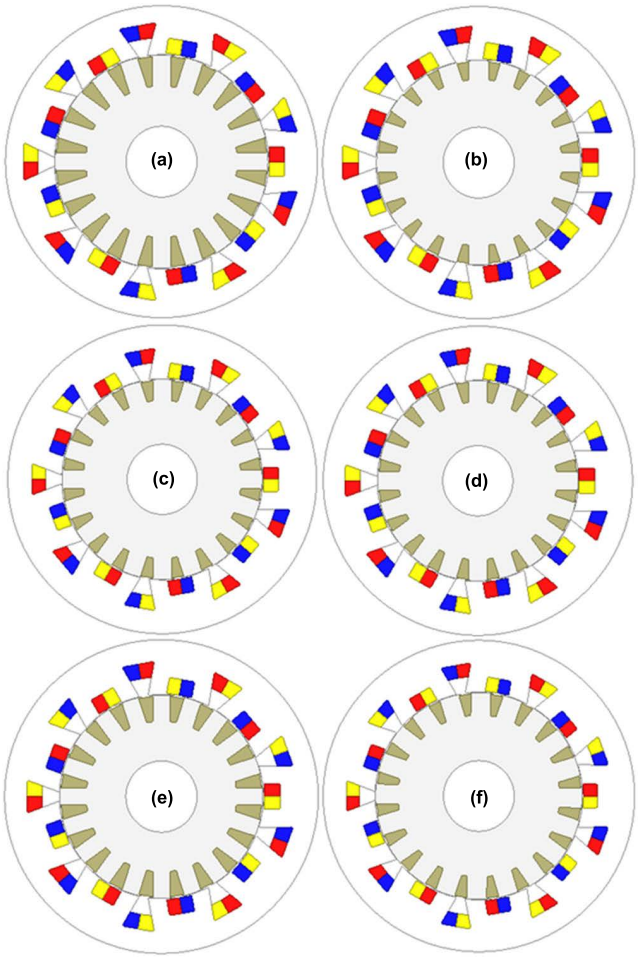

FIGURE 18. 2-D views of 18S/20R/6P AIMs. (a) Initial. (b) Individual optimized. (c) SOGO with J_S restriction. (d) SOGO with P_{Scu} restriction. (e) MOGO with J_R restriction. (f) MOGO without J_R restriction.

By using a closed-rotor structure, parasitic effects and bar copper loss caused by the highly distorted air-gap flux density waveform may be reduced, and the FW capability of the AIMs can be improved by extending the stack length. In order to determine the best slot geometry, the influence of rotor slot shape on the SS and FW performances, four different rotor structures namely; insert-bar, (IB), open-slot cast-rotor (OS), closed-slot cast-rotor with straight bridge (SB), and closed-slot cast-rotor with u-shaped bridge (uB) have been investigated. Furthermore, the stack length of AIM has been expanded from 70mm to 105mm in order to improve its FW capability. Note that once the stack length of AIM is equal to 105mm, its total axial length becomes equal to its CIM counterpart. In this regard, an attempt was made to establish a balance between number of turns and stack length in terms of the improvement of FW capability.

A. ROTOR SLOT SHAPE IMPROVEMENT

The most significant improvements have been reported to be accomplished by modifying the rotor slot design, which can decrease the rotor's bar losses to a minimum [34].

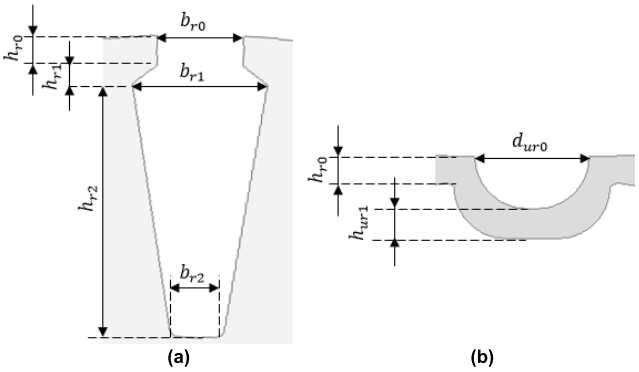

FIGURE 19. Rotor slot geometry. (a) Slot dimensions. (b) Bridge parameters.

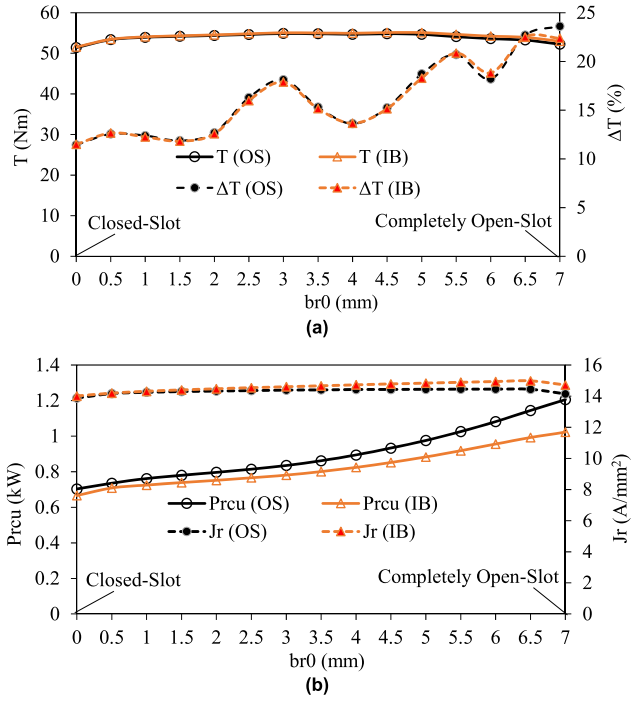

FIGURE 20. Variation of major electromagnetic performance characteristics with b_{r0}. (a) Time-averaged torque and torque ripple. (b) Rotor bar copper loss and bar current density.

The influence of the rotor slot-geometry parameters on the performance characteristics has been investigated by using the specifications of the globally optimized AIM design (e) (see Table 9). Fig. 19(a) shows the geometric parameters of the initial rotor slot design. Note that the initial slot geometry belongs to the insert-bar (IB) topology. In addition, by changing the additional slot opening parameters, shown in Fig. 19(b), straight bridge (SB) and closed-slot cast-rotor with u-bridge (uB) rotor topologies (see Fig. 22(d)) can be formed. Moreover, it is feasible to achieve open-slot cast-rotor (OS) structures by modifying the rotor slot fill factor of the IB structure (see Fig. 22).

The influence of the aforementioned slot geometry parameters on the SS performance of AIMs having IB and OS

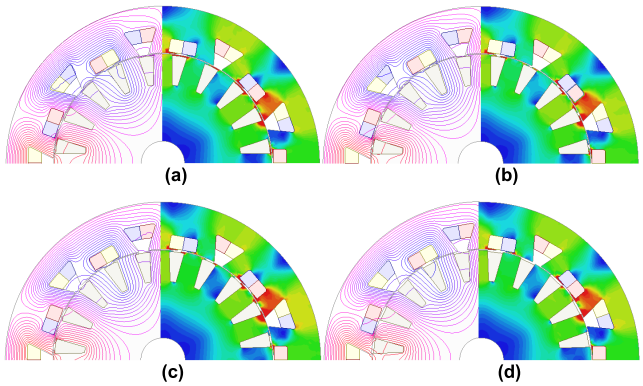

FIGURE 21. Flux line and flux density distributions for various widths of b_{r0}. (a) b_{r0} = 0mm (closed-slot). (b) b_{r0} = 1.5mm (semi-closed-slot). (c) b_{r0} = 3.5mm (semi-closed-slot). (d) b_{r0} = 7mm (open-slot). (Note that see Fig. 27. for the scale of the magnetic flux density distributions.)

rotors have been investigated as follows. The variations of the average torque T, torque ripple ΔT, rotor bar copper loss P_{rcu}, and bar current density J_r with b_{r0} are shown in Fig. 20. It has been revealed that although the amplitudes of T and J_r are not changed considerably, ΔT and P_{rcu} are increased as b_{r0} increases. It has been deduced that b_{r0} should be small as feasible as possible to keep P_{rcu} and ΔT values at the minimum. Fig. 21 depicts the flux line and flux density distributions for varying values of b_{r0}. Some heavily saturated local parts can be observed, particularly at tooth body and tip parts. In addition, as seen in Fig. 21(a), through the iron bridges, some of the flux is short-circuited. The flux density on the open-slot rotor, on the other hand, is decreased because it cannot collect flux as well as the semi-closed-slot rotor (see Fig. 21(d)). Therefore, as shown in Fig. 20(a), AIMs with the closed- and open-slot rotors have lower average torque.

1) SQUIRREL-CAGE TOPOLOGIES

The squirrel-cage rotor can be designed in a variety of ways depending upon the rotor manufacturing, as illustrated in Fig. 22. In terms of construction, the rotor may be made in two ways: insert-bar and cast-rotor. The cast-rotor manufacturing is less complicated than insert-bar manufacturing. In essence, the cast-rotor type can be manufactured as open- and closed-slot as shown in Fig. 22.

The rotor of the AIM is designed by utilizing these six different rotor topologies. Note that, except for b_{r0}, h_{r0}, and h_{r1} and additional slot bridge parameters shown in Fig. 19(b), all of the specifications are preserved at their optimal values. The AIMs designed with the rotor slot types shown in Fig. 22 were compared to the CIM with an IB rotor structure in terms of SS and FW performance.

2) COMPARISON OF SS PERFORMANCE

A comparison study of the major SS electromagnetic characteristics of the AIM equipped with various rotor designs and the CIM equipped with the IB rotor was conducted

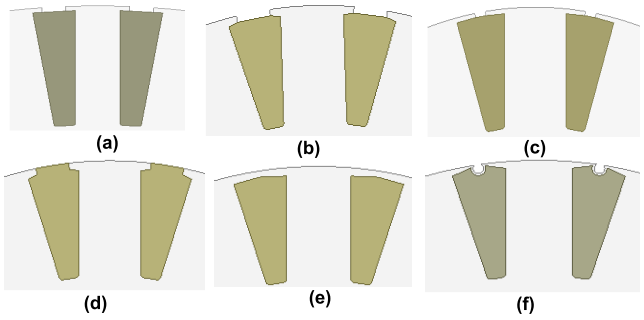

FIGURE 22. Various rotor slot types having different shapes. (a) Insert-bar of CIM–IB (CIM). (b) Insert-Bar with large slot opening (IB1). (c) Insert-bar with optimum slot opening (IB2). (d) Open-slot cast-rotor (OS). (e) Closed-slot cast-rotor (straight bridge - SB). (f) Closed-Slot Cast-Rotor (u-Bridge - uB).

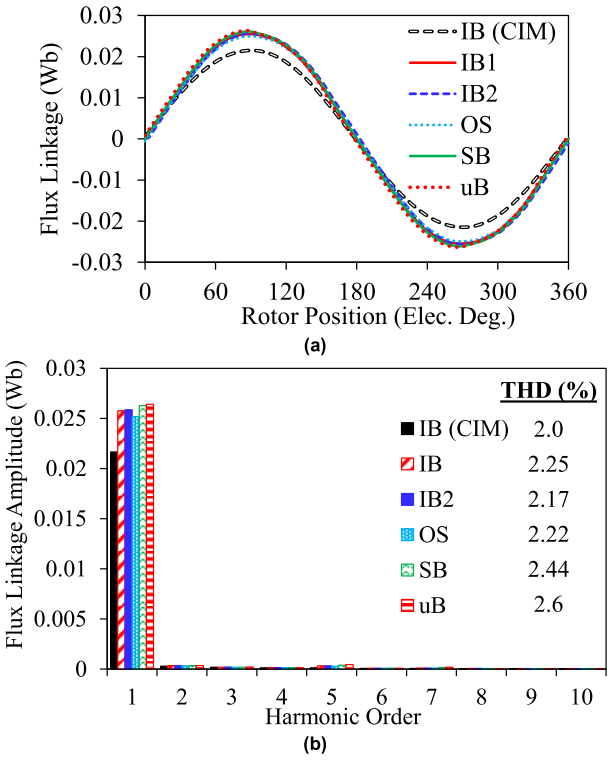

FIGURE 23. Flux-linkage. (a) Waveform. (b) Harmonic spectra.

in this section. The effect of rotor types was investigated based on the 18S/20R/6P AIM and the 54S/44R/6P CIM. The major rotor slot parameters are listed in Table 11, and the cross-sectional views of the rotors are shown in Fig. 22.

Fig. 23 shows the flux-linkage waveforms and associated harmonic spectra. As seen, the flux linkage amplitude of the CIM is smaller than that of the AIMs with different rotor topologies due to its low number of turns. It is also evident that there is no discernible variation in the distortion levels. The 'Phase A' induced voltage waveforms as well as their harmonic spectra are illustrated in Fig. 24. The waveforms of the designs with ANW topology are more

TABLE 11. Rotor slot parameters.

	CIM	AIM				
Spec. (mm)	IB	IB1	IB2	OS	SB	uB
b_{r0}	2	4.4	1.5	4.4	0	0
t h_{r0}	0.5	0.8	0.5	0.8	0.2	0.2
h_{r1}	0	0.4	0.3	0.4	0.6	0.6
b_{r12}	2.68	6	6	6	6	6
h_{r2}	12.6	12.58	12.58	12.58	12.58	12.58
d_{ur0} / h_{ur1}	—	—	—	—	—	12/0.5

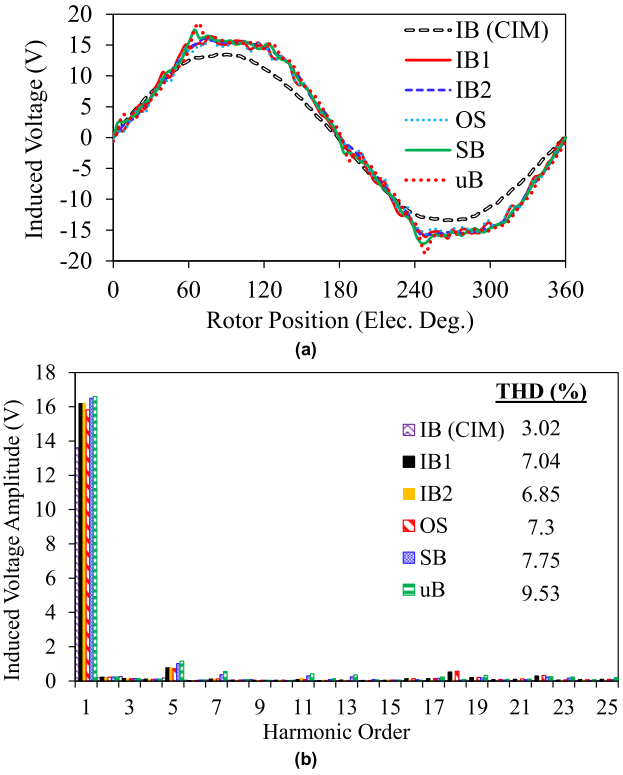

FIGURE 24. Induced voltage. (a) Waveforms. (b) Harmonic spectra.

distorted than those of the CIM as a consequence of having more winding MMF harmonic contents. The THDs of the AIMs are substantially greater than those of the CIM, as seen in Fig. 24(b). Furthermore, AIMs with a closed slot rotor structure have greater THD levels than their open slot counterparts.

Fig. 25 depicts the air-gap flux density waveforms and associated harmonic spectra. Nonetheless, because the AIMs' MMF waveforms are highly distorted, their THD levels are greater than those of CIM. Furthermore, as shown in Fig. 25(b), the THD level of the AIM with a closed rotor structure has been decreased primarily as a result of the bridges' filtering effect. In [56], it has been shown that rotor tooth parts act as a low-pass filter, leading to the higher frequency harmonics being gradually eliminated. Therefore, in the same manner, the rotor slot bridges act as low-pass filter and prevent high-frequency field harmonics to induce in the rotor bars. Consequently, a lower bar copper loss can also be predicted for AIMs with closed rotor slot types.

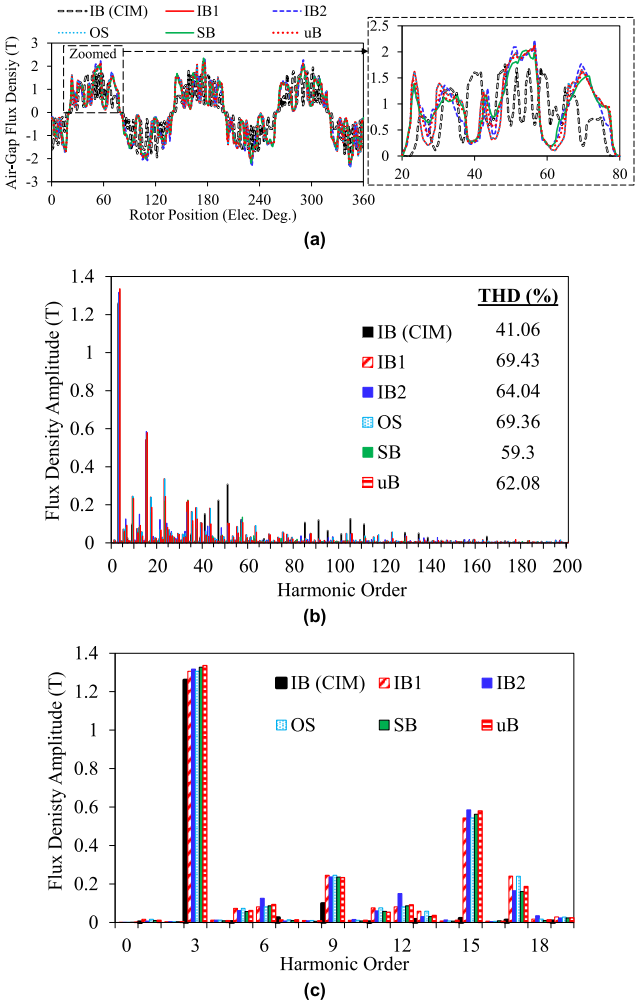

FIGURE 25. Air-gap flux density. (a) Waveforms. (b) Harmonic spectra. (c) Low-order harmonics.

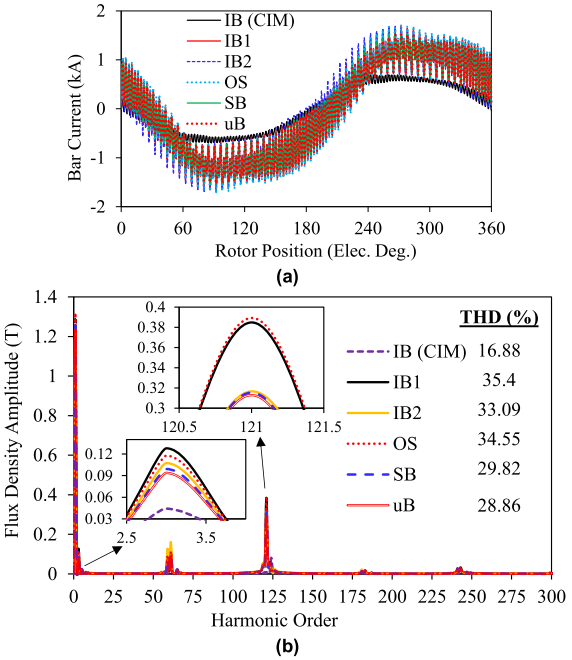

FIGURE 26. Rotor bar current. (a) Waveforms. (b) Harmonic spectra.

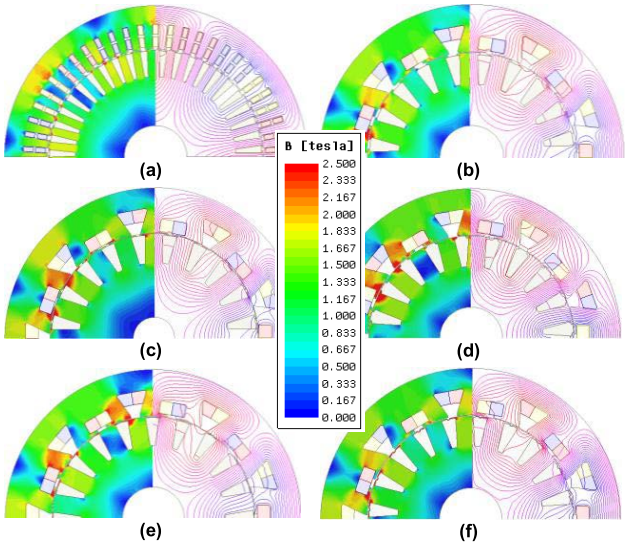

FIGURE 27. Flux density and flux line distributions. (a) 54S/44R/6P CIM (IB). (b) 18S/20R/6P (IB1). (c) 18S/20R/6P (IB2). (d) 18S/20R/6P (OS). (e) 18S/20R/6P (SB). (f) 18S/20R/6P (uB).

The MMF harmonics are induced in air-gap field and then in the rotor bars. Thus, the distortion level of the bar current of the AIMs are much higher than that of the CIM as seen in Fig. 26. It is also clear that the bar-current THD levels of designs with closed rotor slots are significantly lower than those of designs with open rotor slots. Both of the low- and high-order harmonics have been reduced thanks to the slot bridges. Moreover, as aforementioned, these bar current harmonics result in a rise in rotor bar copper losses (see Fig. 33). The use of the u-bridge results in a reduction in the saturation level of the stator teeth parts, as seen in Fig. 27. In addition, short-circuited fluxes via the bridges can be seen in Fig. 27(d) and (e). This explains why designs with closed slot rotors have lower torque (see Fig. 29).

Non-sinusoidal or trapezoidal waveforms are present in all waveforms, as well as a huge number of high order harmonics. The causes of non-sinusoidal bar current waveforms, including slip, electric loading, S/P/R combinations, rotor skew, air-gap length, slot geometric dimensions, etc., have been thoroughly examined in [27]–[29] and [56]. It has been reported in [27] that saturation of the rotor tooth body parts causes the rotor bar current waveform to be trapezoidal.

The bars' total loss distributions, calculated by taking into account the copper and eddy current losses, are compared in Fig. 28. The losses, concentrated on the top parts of the bar conductors, is due to the combined effects of the deep slot, skin, air-gap flux density, and hence MMF harmonics. The copper loss is increased because these high-distorted air-gap flux density harmonics are induced in the top portion

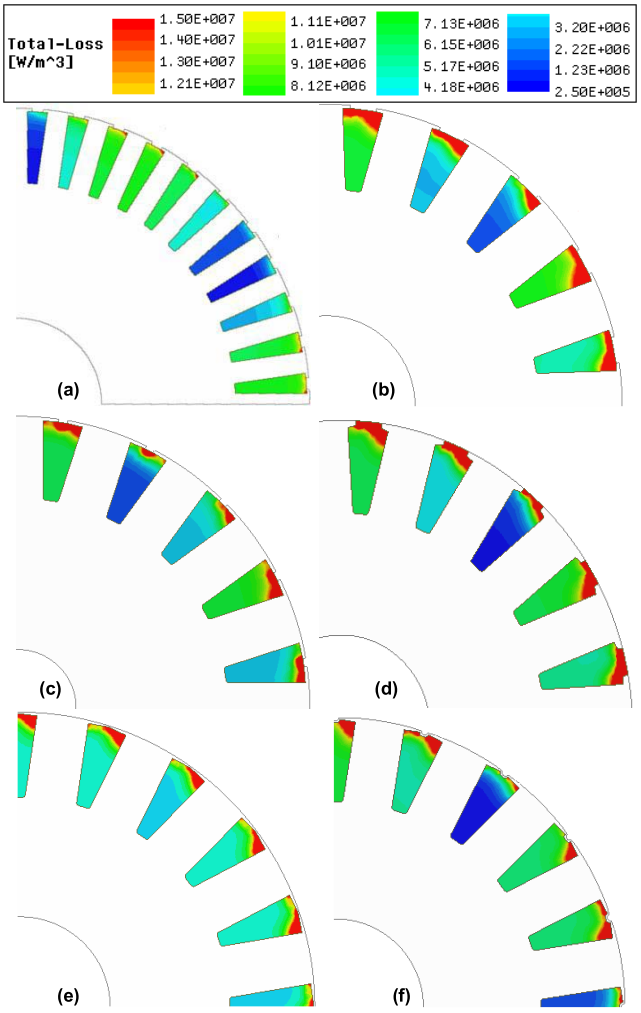

FIGURE 28. Total loss distributions on the rotor bars. (a) 54S/44R/6P CIM (IB). (b) 18S/20R/6P (IB1). (c) 18S/20R/6P (IB2). (d) 18S/20R/6P (OS). (e) 18S/20R/6P (SB). (f) 18S/20R/6P (uB).

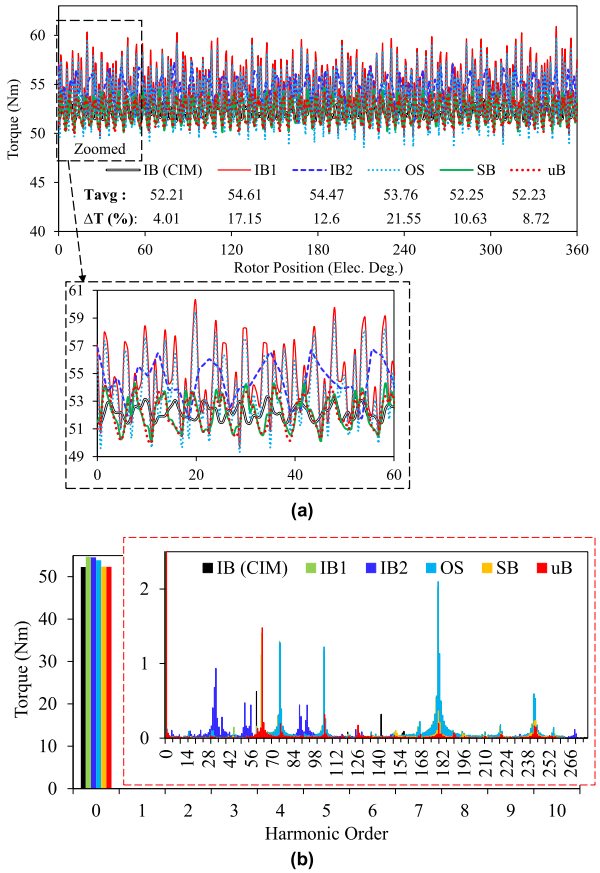

FIGURE 29. Electromagnetic torque. (a) Waveforms. (b) Harmonic spectra.

of the bars. The overall loss level, on the other hand, has been diminished due to the slot bridges, as shown in Fig. 28(d) and (e). It is also evident that the overall loss of the u-bridge (uB) design is smaller than that of the straight-bridge design (SB). The current density reaches its highest at the top of the bar and falls to its minimum at the bottom due to the lower bar's greater reactance. The air-gap flux density harmonics create eddy currents in the copper bars at the slot necks of the IB rotor. By utilizing a bridge into the top of the rotor slots, the bar conductor is shifted away from the air-gap and hence the cage losses are further reduced (see Fig. 28(d) and (e)). When a u-bridge is used instead of a straight-bridge, the bar conductors are moved further away from the air gap, resulting in a greater decrease in bar loss. On the other hand, the rotor structure's mechanical durability is diminished, which may exclude the usage of slot-bridge designs in super-high-speed IMs.

Fig. 29 shows the computed electromagnetic torque in relation to the rotor position. There are large disparities in the torque ripple ranges, despite the fact that there are no significant variances between the average torque values. However, as previously stated, the average torque for AIMs with slot bridges is significantly reduced due to an increase in short-circuited flux across the rotor slot bridges. The slot bridges, on the other hand, result in a considerable reduction in torque ripple. The rotor slot bridges cancel out more than half of the torque ripple, as seen in the figure. When compared to the SB rotor structure, the uB rotor structure achieved an additional torque ripple reduction of ∼18%.

3) COMPARISON OF FW PERFORMANCE

The FW characteristics were estimated using a technique that combined FEA-calculated flux-linkage and power loss matrices with MATLAB®-calculated current angle and speed loops. The torque-and power-speed curves, rotor and stator copper loss maps, and efficiency maps are calculated according to the aforementioned method and presented as follows.

Fig. 30 shows the torque-speed characteristics of the CIM with IB and the NWIMs with IB, OS, SB, and uB. Although the CIM's performance in the constant torque region is poor, it performs admirably in the constant power region. On the other hand, it has been revealed that the rotor structure

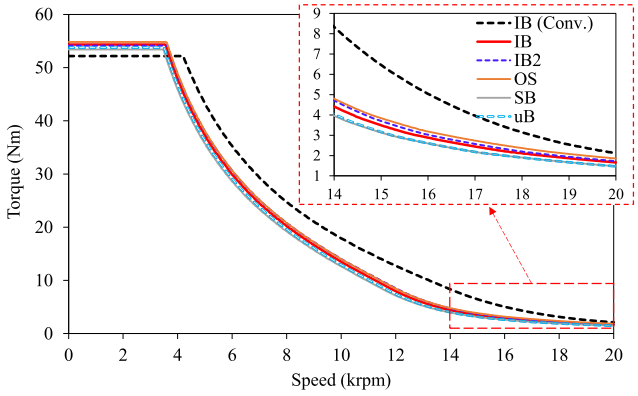

FIGURE 30. Torque-speed characteristics.

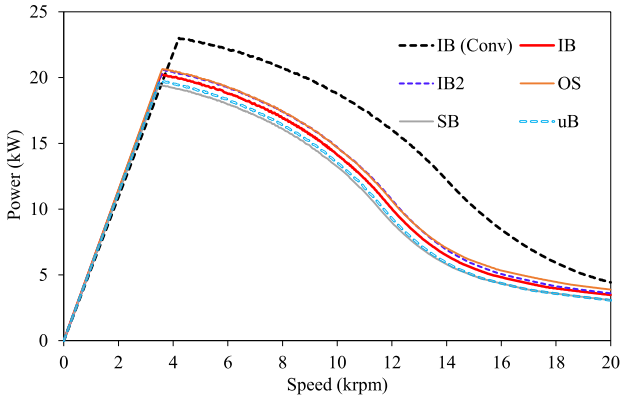

FIGURE 31. Power-speed characteristics.

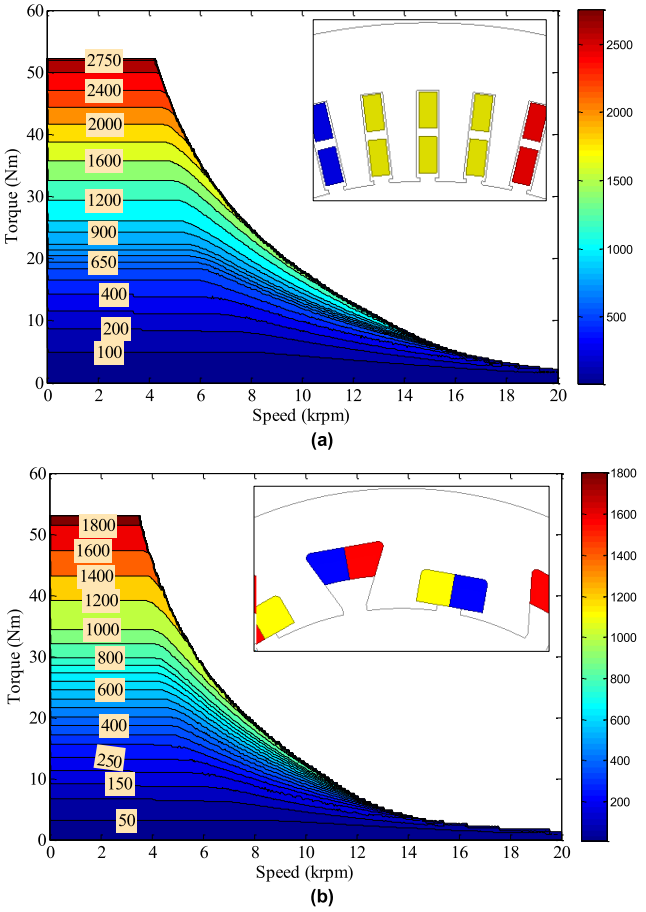

FIGURE 32. Stator copper loss maps. (a) CIM. (b) AIMs.

has a trivial effect on the FW performance. The overall performance of the rotors with bridges is slightly poorer than that of the open slot rotor structure. In Fig. 31, the power-speed curves of the IMs are compared. The CIM clearly has the highest power throughout the whole operational speed range. The power-speed characteristics of rotor constructions with bridges are marginally worse than those of rotor structures with open slots. Fig. 32 depicts the CIM and AIM copper loss maps. The stator copper losses of the AIMs with varied rotor structures are relatively comparable, as shown in Fig. 32(b), since only the rotor structure has been modified, while all other parts have been kept at their optimum. The AIM's maximum copper losses at constant torque are 32.15% lower than that of the CIM due to the AIM's extremely short end-winding lengths.

Fig. 33 illustrates the calculated rotor bar copper loss maps. Although the CIM has an open-slot rotor design, its bar copper loss is lower than the AIMs due to the lower MMF and hence lower air-gap flux density, as seen in Fig. 33(a). Although the design with the OS has the highest bar loss in the constant torque area, the design with the uB has the lowest, as shown in Fig. 33(b-e). Some high-order air-gap flux density harmonics were finally eliminated because the slot bridges operate as a low-pass filter. As a result, certain copper losses caused by MMF harmonics on the bars have been eliminated. Additional losses like as stray current loss, mechanical losses, and so on were included into the efficiency maps of the evaluated IMs. The additional losses are estimated to be 1% of the output power [53]. The CIM's maximum efficiency is 92%, which was reached between 5krpm −9krpm. Furthermore, at 0−0.75krpm, the zone with the lowest efficiency (<55%) is found (see Fig. 34(a)). Fig. 34(b-e) shows the efficiency maps of the AIMs with IB, OS, SB, and uB, respectively. The designs with slot bridges are clearly more efficient than the designs without slot bridges.

The maximum efficiency zones for open-slot designs are smaller (see Fig. 34(b) and (c)). The greatest efficiency zones, however, are bigger, as shown in Fig. 34(d) and (e). Furthermore, between 5-8krpm, the maximum efficiency is raised from 92% to 93% owing to the uB. Furthermore, the highest efficiency zone of AIM with uB is far greater than that of the CIM. When comparing the CIM and AIM with uB, it can be shown that the NWIM's efficiency with uB is significantly higher. An EV spends the majority of its time in cruise/city mode (low-torque and low-speed operating region). Consequently, achieving great efficiency in cruise mode operating is desirable. The AIM with uB clearly surpasses the CIM in terms of efficiency, and, as a

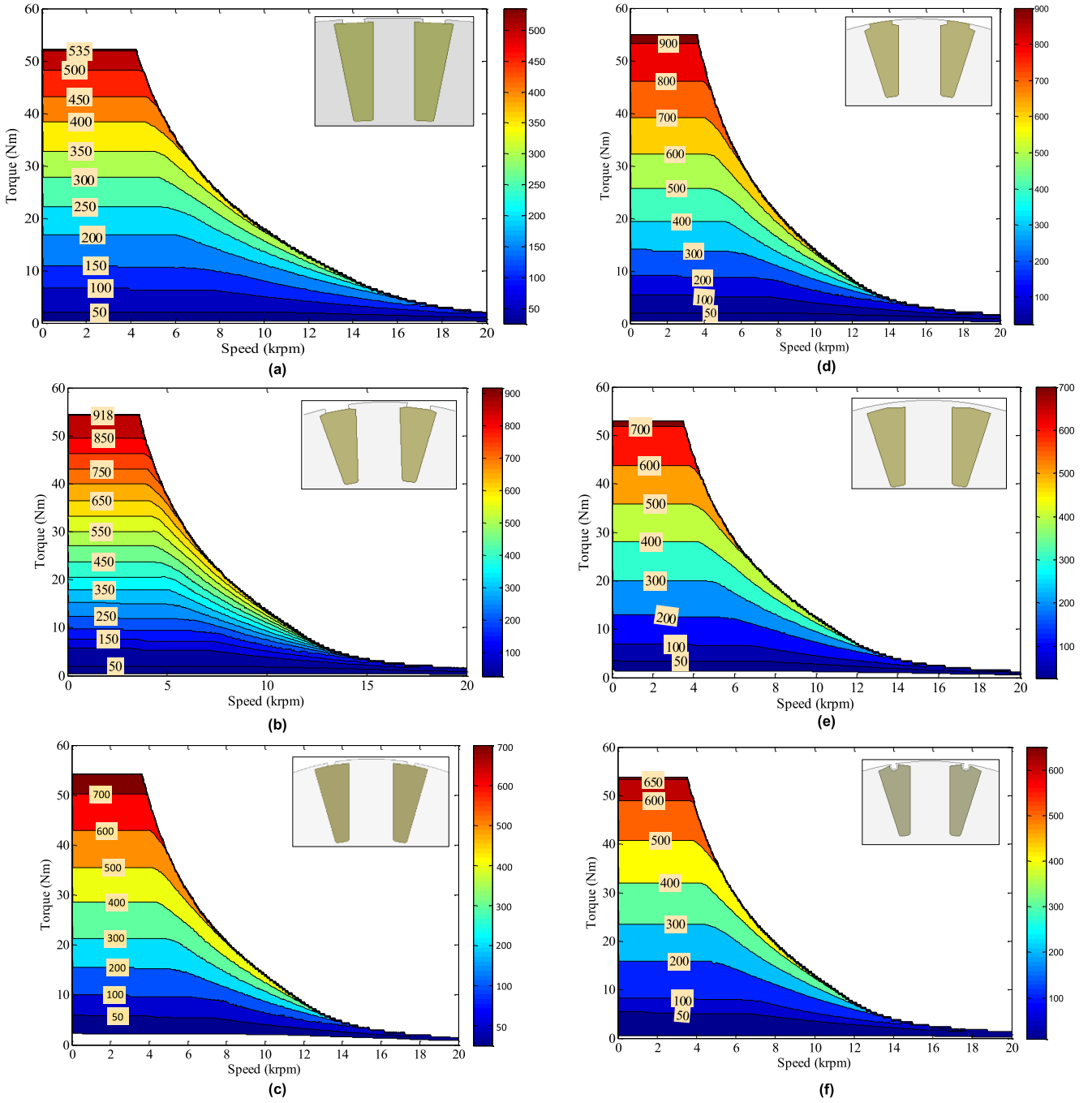

FIGURE 33. Rotor bar copper loss maps of CIM and AIMs. (a) IB (CIM). (b) IB1. (c) IB2. (d) OS. (e) SB. (f) uB.

result, fuel/energy economy, as shown in Fig. 34(a) and (e). Moreover, the AIM with uB is more compact than the CIM since its total axial length is 15% less (see Table 12). Although using bridges for rotor slots reduces torque and hence power, it increases efficiency, as seen in the figures. The efficiency of the rotor may be improved further by altering the geometric parameters. In future work, the impact of rotor slot parameters on AIMs will be further examined.

4) OVERALL PERFORMANCE COMPARISON

Table 12 is presented to compare the overall SS characteristics. In the table, R, l_s, l_{end}, l_{total}, k_{wp}, R_{phase}, n_{maxT}, T, ΔT, P_{out}, P_{Scu_in}, P_{Scu_end}, P_{Scu}, P_{Rcu}, P_{hyst}, P_{eddy}, J_S, and J_R specify the number of rotor slots, stack length, end-winding axial length, total axial length, fundamental winding factor, phase resistance with 0.63 slot fill factor, pull-out rotor speed, torque, torque ripple, output power, stator slot copper loss, end-winding copper loss, total stator

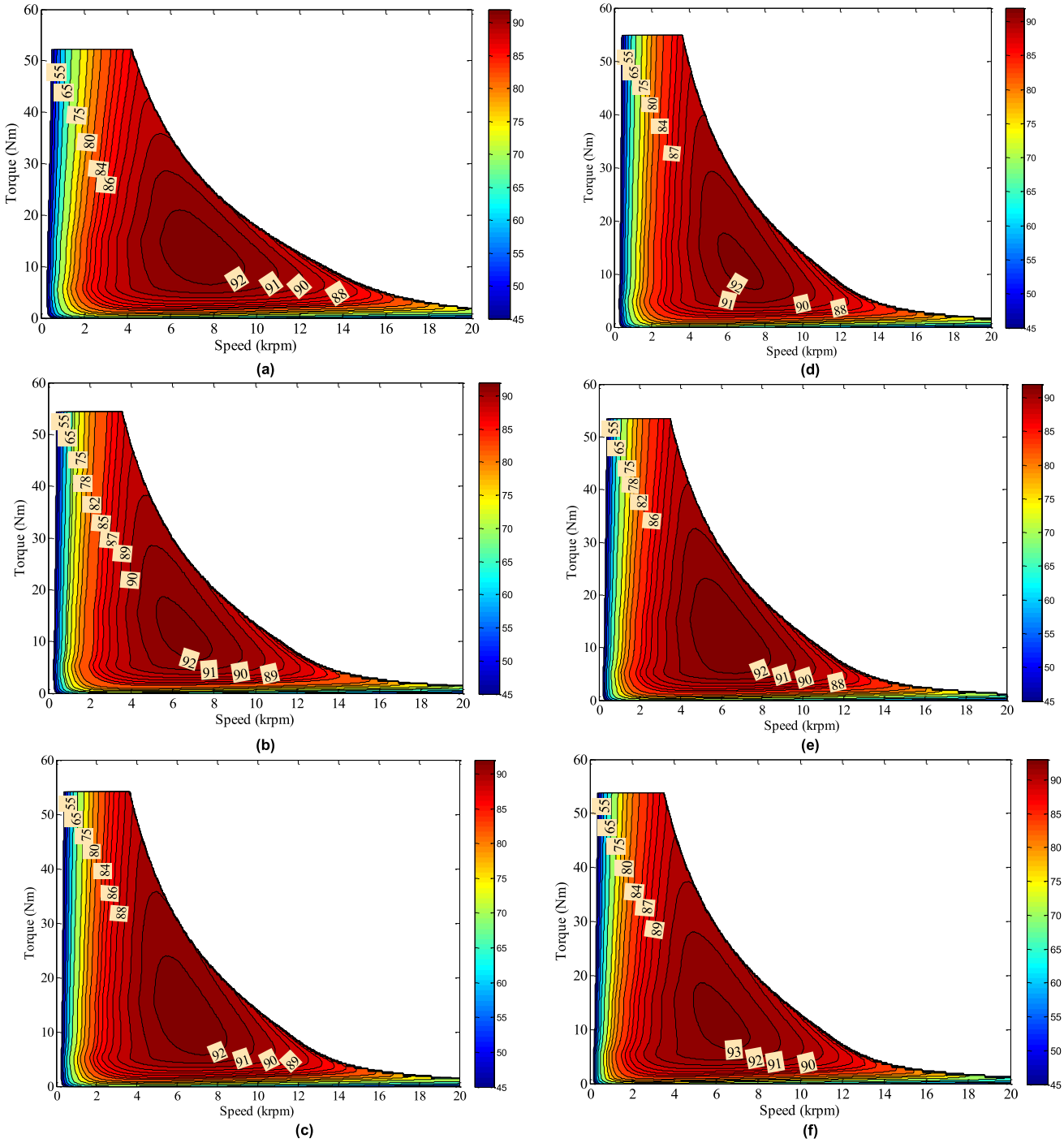

FIGURE 34. Efficiency maps of CIM and AIMs. (a) IB (CIM). (b) IB1. (c) IB2. (d) OS. (e) SB. (f) uB.

copper loss, rotor bar loss, hysteresis loss, core eddy current loss, winding current density, and rotor bar current density, respectively.

The OS rotor offers certain advantages, such as improved torque and efficiency, as well as disadvantages, such as high torque ripple and bar copper loss. It should also be emphasized that fabrication of the IB rotor is more difficult than that of the cast-rotor. On the other hand, it has been revealed that using closed rotor slots can remarkably increase the performance of the AIMs.

The benefits of adopting closed slots may be summarized as follows, based on Table 12:

- ✓ Lower rotor bar copper loss and hence higher efficiency;
- ✓ Lower torque-ripple;
- ✓ Cast-rotor availability (ease of manufacturing);
- ✓ Lower slip and consequently higher power factor;

TABLE 12. Performance characteristics at constant torque region.

Parameters	IB (CIM)	IB	OS	SB	uB
N_t	9		12		
R	44		20		
l_s (mm)	70		70		
l_{end} (mm)	52		10.25		
l_{total} (mm)	122		80.25 **(-34.22%)**		
k_{wp}	0.96		0.866 **(-9.8%)**		
R_{phase} (mΩ)	3.7261		2.5242		
n_{maxT} (rpm)	1905	1905	1905	1910	1915
T (Nm)	52.21	54.66	54.14	53.4	52.5
ΔT (%)	4	17.15 **(+329%)**	21.55 **(+439%)**	10.63 **(+166%)**	8.72 **(+118%)**
P_{out} (kW)	10.41	10.9	10.8	10.68	10.53
P_{Scu_in} (kW)	0.727	1.297	1.297	1.297	1.297
P_{Scu_end} (kW)	2.067	0.596	0.596	0.596	0.596
P_{Scu} (kW)	2.794	1.893	1.893	1.893	1.893
P_{Rcu} (kW)	0.51	0.925	0.988	0.718	0.652
P_{hyst} (W)	68.17	83.78	120.43	126.1	79.35
P_{eddy} (W)	7.92	12.63	14.68	12.35	10.53
J_S (A/mm^2)	22.32	30.96 **(+38.7%)**	30.96 **(+38.8%)**	30.96 **(+38.8%)**	30.96 **(+38.8%)**
J_R (A/mm^2)	13.54	13.71 **(+1.25%)**	14.39 **(+2.36%)**	13.86 **(+2.36%)**	12.9 **(-4.72%)**
Power factor	0.658	0.682	0.654	0.683	0.687

✓ Low current density and hence smaller cooling equipment size.

Closed slots, on the other hand, have the following drawbacks:

- The average torque falls slightly as a result of the bridges increasing the short-circuited flux level;
- The FW performance is slightly reduced due to the closed-slot construction;
- The mechanical durability of a rotor with tin slot-bridges is reduced.

B. INFLUENCE OF STACK LENGTH

Since axial lengths of AIMs are quite short thanks to the nonoverlapping winding topology, increasing the stack length of the machine is another way of improving AIM's poor performance in the constant-power region. In essence, increasing the stack length increases the constant-torque area. However, in the current case, increasing the torque level at constant-torque region is not desired. Therefore, the constant-power region can be enlarged by reducing number of turns per phase.

The previously proposed 18S/20R/6P combination was chosen to examine the effect of axial length on the FW performance of the AIM. The copper loss and efficiency maps were used to compute and compare the FW performance of the proposed AIM with 70mm and 105mm. Note that the 105mm stack length is the maximum stack length that does not exceed the corresponding CIM's total axial length.

1) INFLUENCE ON SS PERFORMANCE

The influence of stack length on the SS performance characteristics have been investigated in [11]. It has been demonstrated that extending the stack length whilst keeping the torque consistent improves overall performance, including power and current densities, efficiency, and parasitic effects like torque ripple, vibration, acoustic noise, etc.

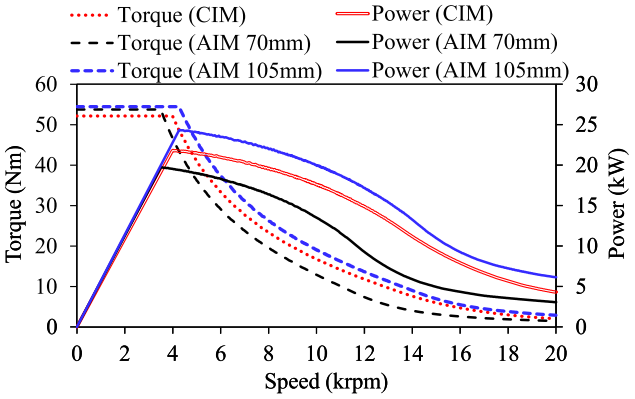

FIGURE 35. Comparison of torque- and power-speed characteristics.

TABLE 13. Performance comparison between CIM and AIMs (% difference).

Parameter	CIM to AIM 70mm	CIM to AIM 105mm	AIM 70mm to AIM 105mm
Total axial length	-34.22	0	52.02
Peak power	-9.62	11.67	23.56
Power @ 10krpm	-24.8	13.43	50.84
Power @ 20krpm	-29	42.32	100.45
Max. stator copper loss	-31.82	-34.91	-4.53
Max. rotor copper loss	22.43	0.93	-17.56
Max. efficiency	1.09	2.17	1.08

2) INFLUENCE OF FW PERFORMANCE

Under the 500Arms and 24Vrms inverter ratings, the FW performance of the considered AIM with various stack lengths was computed and compared with CIM. 70mm, and 105mm have 12, and 8 turns per phase, respectively. The following are the FW characteristics, loss, and efficiency maps that were obtained.

Fig. 35 depicts the CIM's and AIM's torque/power-speed characteristics for 70mm, and 105mm stack lengths. In addition, it illustrates the tradeoff between stack length and power at constant power operating region. It has been found that the increased stack length improves the FW capability remarkably.

Once the stack length is increased and the number of turns is gradually decreased, the power at high-speed regions increases substantially. The loss and efficiency maps of the AIM having 105mm stack lengths are illustrated in Fig. 36. To make a comparison between AIMs with 70mm and 105mm, Fig. 32, Fig. 33, and Fig. 34 show the loss and efficiency maps of AIM with 70mm. On the other hand, a comparison table associated with torque/power-speed and power loss and efficiency maps is given in Table 13. Note that for the percentage comparison, the CIM is considered as the base for the first 2 columns, and the AIM 70 mm is taken as the base for the last column of Table 13. According

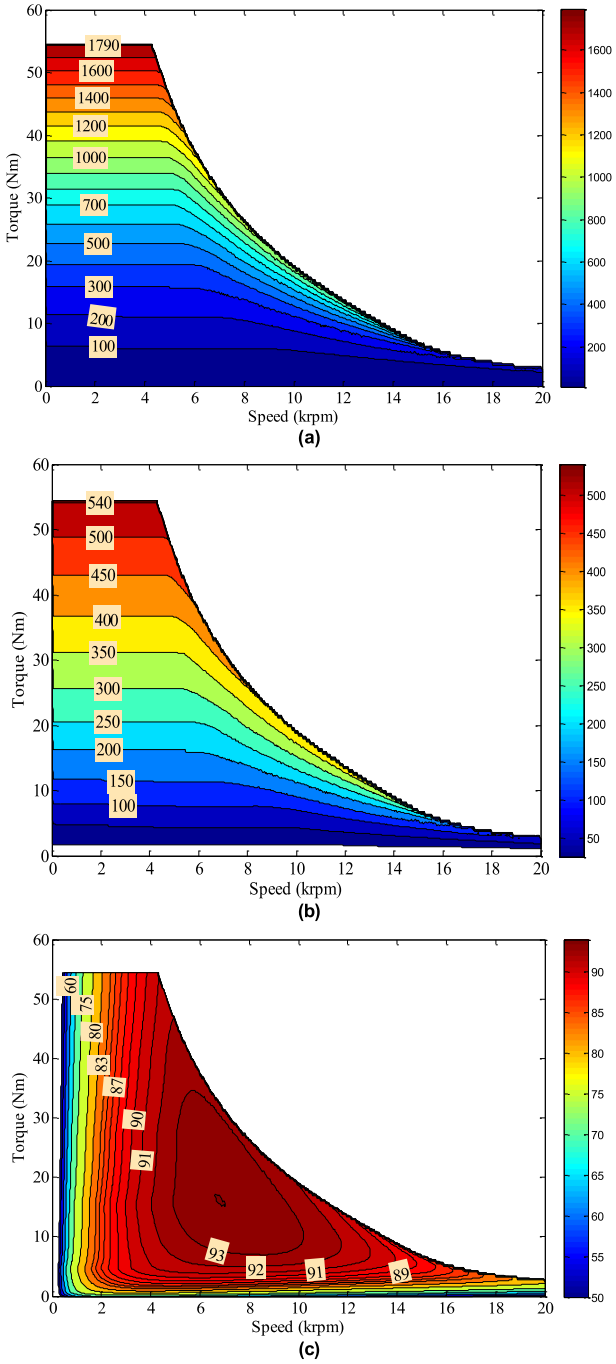

FIGURE 36. Power loss and efficiency maps of AIMs having 105mm. (a) Stator copper loss map. (b) Rotor bar copper loss map. (c) Efficiency map.

to the CIM, the AIM 70mm has 34.22% shorter total axial length with 1.09% higher efficiency. However, its power level at high-speed regions is very low. On the other hand, the CIM with 105mm much higher peak torque and efficiency compared to CIM. In addition, its power at 20krpm is 42.32% higher than that of the CIM. In other words, once the AIM is designed to have the same total axial length with CIM, corresponding to stack length of 105mm, it shows better FW characteristics.

Once the stack length of AIM is increased from 70mm to 105mm, all performance parameters are significantly increased as shown in Table 13. One of the most critical improvements is the increase in power at 20krpm by 100.45%. In addition, the maximum stator copper loss is decreased by 4.53% when the stack length is increased from 70mm to 105mm, since the number of turns per phase is decreased.

VI. CONCLUSION

This paper presents the optimization and further performance improvement of IMs having ANWs for EV/HEV applications. Firstly, the AIM is optimized using single- and multi-objective approaches, as well as individual and global optimization methods. Secondly, for AIMs, two different performance improvement methods consisting of using closed-slot rotor topologies with u-shaped slot bridges in order to reduce parasitic effects and consequently bar copper loss. Moreover, the influence of stack length on FW capability is investigated by taking into account the number of turns per phase. Finally, the SS and FW performance characteristics of the optimized and improved AIM are compared with its conventional counterpart (CIM) in order to reveal the effectiveness of the proposed methods. The followings are some of this study's key findings.

- The SO or MO global optimization approaches have been shown to be highly successful for finding the optimal solution, depending on parameter constraints or justification of objectives.
- Because the simulation and hence the optimization of the IMs take a very long time, using a minimal variable number allows to identify the optimal solution quickly.
- Implementation of uB into the rotor provides reduced torque ripple and bar copper loss, improved power factor and efficiency, reduced slip and current density, smaller cooling equipment requirement, slightly decreased torque, and reduction in the mechanical robustness of rotor.
- Increasing the stack length by maintaining the torque, i.e. reducing the number of turns, provides improved FW characteristics, reduced stator and rotor bar copper loses, and improved efficiency. It is also demonstrated that if the AIM is designed to have same total axial length as CIM, its FW characteristics and efficiency would be better.

APPENDIX

In order to validate the FEA predictions presented in this study, experimental validation for CIM is presented. Although the FEA predictions are commonly assumed to be very reliable, their results may be inaccurate due to human errors in modelling and analysis. As a result, for at least one model, experimental validation of FEA results may be required.

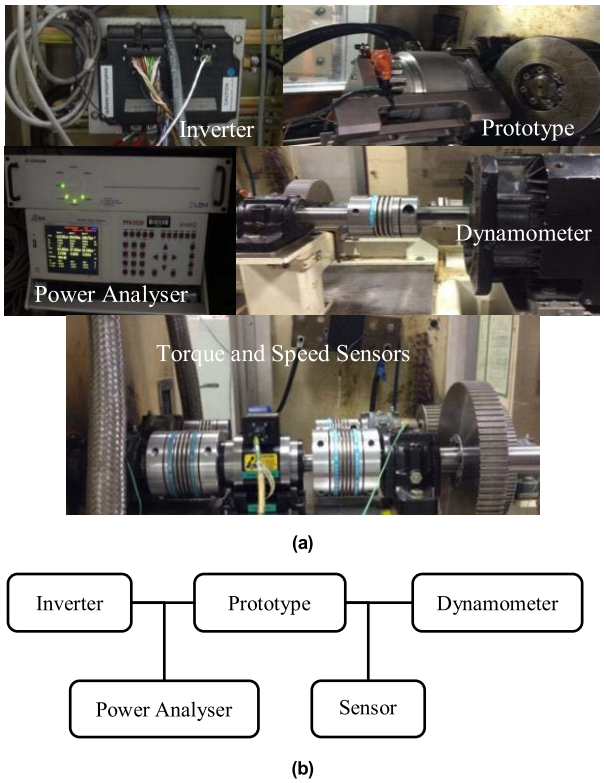

FIGURE 37. Experimental setup. (a) Prototyped IM and test instruments. (b) Schematic of the test rig setup connection.

This section presents the validation of the FEA predicted SS and FW performance characteristics of CIM by measurements. In order to validate the FEA calculations, the prototyped IM's measurement data are collected from [57]. The design dimensions and specifications of the prototyped CIM are given in Table 2.

Fig. 37 illustrates the prototyped CIM, components of the test rig and the connection diagram of the test setup. The highest output torque, as established by the dynamometer, is achieved at a certain rotor speed across the operating speed range while staying within the inverter current and voltage limitations. The power analyser measured the applied voltage and current, input power, current angle, and other parameters. The comparison between FEA predicted and measured SS characteristics, including phase voltage, output torque and power with respect to inverter current, are shown in Fig. 38. Note that the SS measurements have been performed at 1krpm synchronous speed. As clearly seen all the FEA predicted and measured SS data agree quite well. The comparison of the FEA predicted and measured FW characteristics, including torque– and power–speed and efficiency–speed curves are shown in Fig. 39. Note that the FW characteristics have been obtained at maximum inverter rate, which are 500Arms and 48V (DC). It has been observed that a very good agreement between the FEA predicted and measured FW performance characteristics is achieved. As a result of the well-agreed FEA predicted

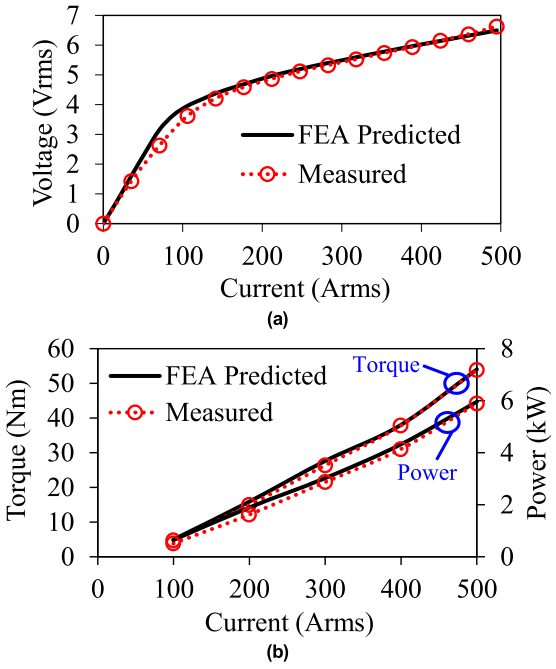

FIGURE 38. SS loading performance. (a) Phase voltage versus inverter current. (b) Torque and power versus inverter current.

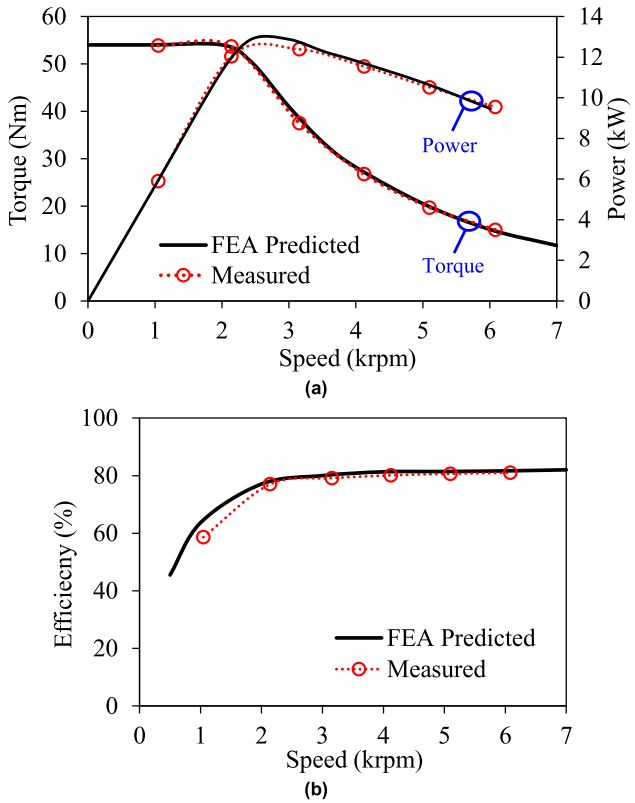

FIGURE 39. FW performance. (a) Torque- and power-speed curve. (b) Efficiency-speed curve.

and measured performance characteristics, the proposed technique, methodology, and analysis results reported in this work are concluded to be reliable.

REFERENCES

[1] H. A. Toliyat, T. A. Lipo, and J. C. White, "Analysis of a concentrated winding induction machine for adjustable speed drive applications. I. Motor analysis," *IEEE Trans. Energy Convers.*, vol. 6, no. 4, pp. 679–683, Dec. 1991, doi: 10.1109/60.103641.

[2] H. A. Toliyat, T. A. Lipo, and J. C. White, "Analysis of a concentrated winding induction machine for adjustable speed drive applications. II. Motor design and performance," *IEEE Trans. Energy Convers.*, vol. 6, no. 4, pp. 684–692, Dec. 1991, doi: 10.1109/60.103642.

[3] H. A. Toliyat and T. A. Lipo, "Analysis of concentrated winding induction machines for adjustable speed drive applications-experimental results," *IEEE Trans. Energy Convers.*, vol. 9, no. 4, pp. 695–700, Dec. 1994, doi: 10.1109/60.368339.

[4] T. Gundogdu, Z. Zhu, and J. Mipo, "Analysis of coil pitch in induction machines for electric vehicle applications," *IET Electric Power Appl.*, vol. 14, no. 12, pp. 2525–2536, Oct. 2020, doi: 10.1049/iet-epa.2019.0980.

[5] V. M. Sundaram and H. A. Toliyat, "A fractional slot concentrated winding (FSCW) configuration for outer rotor squirrel cage induction motors," in *Proc. IEEE Int. Electric Mach. Drives Conf. (IEMDC)*, May 2015, pp. 20–26, doi: 10.1109/IEMDC.2015.7409031.

[6] G. Dajaku, S. Spas, X. Dajaku, and D. Gerling, "An improved fractional slot concentrated winding for low-poles induction machines," in *Proc. Int. Conf. Electr. Mach. (ICEM)*, Lausanne, Switzerland, Sep. 2016, pp. 114–119.

[7] O. Moros and D. Gerling, "Geometrical and electrical optimization of stator slots in electrical machines with combined wye-delta winding," in *Proc. Int. Conf. Electr. Mach. (ICEM)*, Berlin, Germany, Sep. 2014, pp. 2026–2030.

[8] B. B. Jensen, A. G. Jack, G. J. Atkinson, and B. C. Mecrow, "Performance of a folded-strip toroidally wound induction machine," *IEEE Trans. Ind. Electron.*, vol. 59, no. 5, pp. 2217–2226, May 2012, doi: 10.1109/TIE.2011.2138115.

[9] M. Zhang, F. Eastham, and W. Yuan, "Design and modeling of 2G HTS armature winding for electric aircraft propulsion applications," *IEEE Trans. Appl. Supercond.*, vol. 26, no. 3, pp. 1–5, Apr. 2016, doi: 10.1109/TASC.2016.2539548.

[10] T. Gundogdu, "Advanced non-overlapping winding induction machines for electrical vehicle applications," Ph.D. dissertation, Dept. Electron. Elect. Eng., Sheffield Univ., Sheffield, U.K., 2018.

[11] T. Gundogdu, Z.-Q. Zhu, and J.-C. Mipo, "Design and analysis of advanced nonoverlapping winding induction machines for EV/HEV applications," *Energies*, vol. 14, no. 20, p. 6849, Oct. 2021, doi: 10.3390/en14206849.

[12] C. G. Veinott, "Induction machinery design being revolutionized by the digital computer," *Trans. Amer. Inst. Electr. Eng. III, Power App. Syst.*, vol. 75, no. 3, pp. 1509–1517, Jan. 1956.

[13] M. S. Erlicki and J. Appelbaum, "Optimized parameter analysis of an induction machine," *IEEE Trans. Power App. Syst.*, vol. PAS-84, no. 11, pp. 1017–1024, Nov. 1965.

[14] R. Ramarathnam and B. G. Desai, "Optimization of polyphase induction motor design: A nonlinear programming approach," *IEEE Trans. Power App. Syst.*, vol. PAS-90, no. 2, pp. 570–578, Mar. 1971.

[15] J. Buschbeck, M. Vogelsberger, A. Orellano, and E. Schmidt, "Pareto optimization in terms of electromagnetic and thermal characteristics of air-cooled asynchronous induction machines applied in railway traction drives," *IEEE Trans. Magn.*, vol. 52, no. 3, pp. 1–4, Mar. 2016.

[16] N. Zhao and N. Schofield, "An induction machine design with parameter optimization for a 120-kW electric vehicle," *IEEE Trans. Transport. Electrific.*, vol. 6, no. 2, pp. 592–601, Jun. 2020, doi: 10.1109/TTE.2020.2993456.

[17] B. Singh, B. Singh, S. Murthy, and C. Jha, "Experience in design optimization of induction motor using 'SUMT' algorithm," *IEEE Trans. Power App. Syst.*, vol. PAS-102, no. 10, pp. 3379–3384, Oct. 1983.

[18] W. Jazdzynski, "Multicriterial optimisation of squirrel-cage induction motor design," *IEE Proc. B Electr. Power Appl.*, vol. 136, no. 6, pp. 299–307, Nov. 1989.

[19] M.-K. Kim, C.-G. Lee, and H.-K. Jung, "Multiobjective optimal design of three-phase induction motor using improved evolution strategy," *IEEE Trans. Magn.*, vol. 34, no. 5, pp. 2980–2983, Sep. 1998.

[20] M. Çunkas, "Intelligent design of induction motors by multiobjective fuzzy genetic algorithm," *J. Intell. Manuf.*, vol. 21, no. 4, pp. 393–402, Nov. 2008.

[21] J. A. Malagoli, J. R. Camacho, and M. V. F. da Luz, "Optimal design variables to minimize the cost of materials the stator of asynchronous machine," *J. Control, Autom. Electr. Syst.*, vol. 27, no. 2, pp. 157–168, Apr. 2016.

[22] R. Ramarathnam, B. G. Desai, and V. S. Rao, "A comparative study of minimization techniques for optimization of induction motor design," *IEEE Trans. Power App. Syst.*, vol. PAS-92, no. 5, pp. 1448–1454, Sep. 1973.

[23] L. Tutelea and I. Boldea, "Induction motor electromagnetic design optimization: Hooke Jeeves method versus genetic algorithms," in *Proc. 12th Int. Conf. Optim. Electr. Electron. Equip.*, Brasov, Romania, May 2010, pp. 485–492.

[24] A. M. Silva, F. J. T. E. Ferreira, M. V. Cistelecan, and C. H. Antunes, "Multiobjective design optimization of generalized multilayer multiphase AC winding," *IEEE Trans. Energy Convers.*, vol. 34, no. 4, pp. 2158–2167, Dec. 2019, doi: 10.1109/TEC.2019.2935009.

[25] D. A. Souza, W. C. P. A. Filho, and G. C. D. Sousa, "Adaptive fuzzy controller for efficiency optimization of induction motors," *IEEE Trans. Ind. Electron.*, vol. 54, no. 4, pp. 2157–2164, Aug. 2007.

[26] X. Wu, W. Huang, Y. Zhao, and C. Huang, "An efficient model predictive torque control for induction motors with flexible duty ratio optimization," *IEEE J. Emerg. Sel. Topics Power Electron.*, early access, Jul. 8, 2021, doi: 10.1109/JESTPE.2021.3100920.

[27] T. Gundogdu, Z. Q. Zhu, J. C. Mipo, and P. Farah, "Influence of magnetic saturation on rotor bar current waveform and performance in induction machines," in *Proc. Int. Conf. Elect. Mach. (ICEM)*, Lausanne, Switzerland, Sep. 2016, pp. 391–397.

[28] T. Gundogdu, Z. Q. Zhu, and J. C. Mipo, "Influence of stator slot and pole number combination on rotor bar current waveform and performance of induction machines," in *Proc. 20th Int. Conf. Electr. Mach. Syst. (ICEMS)*, Sydney, NSW, Australia, Aug. 2017, pp. 1–6.

[29] T. Gundogdu, Z. Q. Zhu, and J. C. Mipo, "Influence of rotor slot number on rotor bar current waveform and performance in induction machines," in *Proc. 20th Int. Conf. Electr. Mach. Syst. (ICEMS)*, Sydney, NSW, Australia, Aug. 2017, pp. 1–6.

[30] H. Li and K. W. Klontz, "Rotor design to reduce secondary winding harmonic loss for induction motor in hybrid electric vehicle application," in *Proc. IEEE Energy Convers. Congr. Exposit. (ECCE)*, Milwaukee, WI, USA, Sep. 2016, pp. 1–6.

[31] N. Kunihiro, K. Nishihama, M. Iizuka, K. Sugimoto, and M. Sawahata, "Investigation into loss reduced rotor slot structure by analyzing local behaviors of harmonic magnetic fluxes in inverter-fed induction motor," *IEEE Trans. Ind. Appl.*, vol. 53, no. 2, pp. 1070–1077, Mar. 2017.

[32] A. Marfoli, M. D. Nardo, M. Degano, C. Gerada, and W. Chen, "Rotor design optimization of squirrel cage induction motor—Part I: Problem statement," *IEEE Trans. Energy Convers.*, vol. 36, no. 2, pp. 1271–1279, Jun. 2021, doi: 10.1109/TEC.2020.3019934.

[33] A. Lordoglu, M. O. Gulbahce, and D. A. Kocabas, "A comprehensive disturbing effect analysis of multi-sectional rotor slot geometry for induction machines in electrical vehicles," *IEEE Access*, vol. 9, pp. 49590–49600, 2021, doi: 10.1109/ACCESS.2021.3068821.

[34] H.-P. Nee, "Rotor slot design of inverter-fed induction motors," in *Proc. 7th Int. Conf. Electr. Mach. Drives*, Durham, U.K., 1995, pp. 52–56.

[35] A. Marfoli, M. DiNardo, M. Degano, C. Gerada, and W. Jara, "Squirrel cage induction motor: A design-based comparison between aluminium and copper cages," *IEEE Open J. Ind. Appl.*, vol. 2, pp. 110–120, 2021, doi: 10.1109/OJIA.2021.3073820.

[36] S. Lie and C. Di Pietro, "Copper die-cast rotor efficiency improvement and economic consideration," *IEEE Trans. Energy Convers.*, vol. 10, no. 3, pp. 419–424, Sep. 1995, doi: 10.1109/60.464863.

[37] Y. Kawase, T. Yamaguchi, Z. Tu, N. Toida, N. Minoshima, and K. Hashimoto, "Effects of skew angle of rotor in squirrel-cage induction motor on torque and loss characteristics," *IEEE Trans. Magn.*, vol. 45, no. 3, pp. 1700–1703, Mar. 2009.

[38] D. Gerada, A. Mebarki, N. L. Brown, K. J. Bradley, and C. Gerada, "Design aspects of high-speed high-power-density laminated-rotor induction machines," *IEEE Trans. Ind. Appl.*, vol. 58, no. 9, pp. 4039–4047, Sep. 2011.

[39] G. Lee, S. Min, and J. P. Hong, "Optimal shape design of rotor slot in squirrel-cage induction motor considering torque characteristics," *IEEE Trans. Magn.*, vol. 49, no. 5, pp. 2197–2200, May 2013.

[40] T. Kobayashi, F. Tajima, M. Ito, and S. Shibukawa, "Effects of slot combination on acoustic noise from induction motors," *IEEE Trans. Mag.*, vol. 33, no. 2, pp. 2101–2104, Mar. 1997.

[41] G. Joksimovic, M. Mezzarobba, A. Tessarolo, and E. Levi, "Optimal selection of rotor bar number in multiphase cage induction motors," *IEEE Access*, vol. 8, pp. 135558–135568, 2020, doi: 10.1109/ACCESS.2020.3004685.
[42] J. Beerten, J. Verveckken, and J. Driesen, "Predictive direct torque control for flux and torque ripple reduction," *IEEE Trans. Ind. Electron.*, vol. 57, no. 1, pp. 404–412, Jan. 2010, doi: 10.1109/TIE.2009.2033487.
[43] A. Stening and C. Sadarangani, "Reduction of synchronous torques in induction machines using asymmetrical rotor slots," in *Proc. Int. Conf. Elect. Mach. Syst. (ICEMS)*, Sapporo, Japan, Oct. 2012, pp. 1–6.
[44] H. Mikami, K. Ide, K. Arai, M. Takahashi, and K. Kajiwara, "Dynamic harmonic field analysis of a cage type induction motor when magnetic slot wedges are applied," *IEEE Trans. Energy Convers.*, vol. 12, no. 4, pp. 337–343, Dec. 1997, doi: 10.1109/60.638870.
[45] J. F. Gieras and J. Saari, "Performance calculation for a high-speed solid-rotor induction motor," *IEEE Trans. Ind. Electron.*, vol. 59, no. 6, pp. 2689–2700, Jun. 2012.
[46] N. Uzhegov, J. Barta, J. Kurfürst, C. Ondrusek, and J. Pyrhönen, "Comparison of high-speed electrical motors for a turbo circulator application," *IEEE Trans. Ind. Appl.*, vol. 53, no. 5, pp. 4308–4317, Sep. 2017.
[47] F. Riganti Fulginei and A. Salvini, "Comparative analysis between modern heuristics and hybrid algorithms," *Int. J. Comput. Math. Electr. Electron. Eng.*, vol. 26, no. 2, pp. 259–268, Apr. 2007.
[48] D. E. Goldenberg, *Genetic Algorithm in Search, Optimization and Machine Learning*. Boston, MA, USA: Addison-Wesley, 1989.
[49] N. Bianchi and S. Bolognani, "Design optimisation of electric motors by genetic algorithms," *IEE Proc.-Electr. Power Appl.*, vol. 145, no. 5, pp. 475–483, Sep. 1998, doi: 10.1049/ip-epa:19982166.
[50] G. Lei, J. Zhu, and Y. Guo, "Design optimization methods for electrical machines," in *Multidisciplinary Design Optimization Methods for Electrical Machines and Drive Systems*. Berlin, Germany: Springer, 2016, doi: 10.1007/978-3-662-49271-0_4.
[51] G. Lei, J. Zhu, Y. Guo, C. Liu, and B. Ma, "A review of design optimization methods for electrical machines," *Energies*, vol. 10, no. 12, p. 1962, Nov. 2017, doi: 10.3390/en10121962.
[52] Z. Q. Zhu and X. Liu, "Individual and global optimization of switched flux permanent magnet motors," in *Proc. Int. Conf. Electr. Mach. Syst. (ICEMS)*, Beijing, China, Aug. 2011, pp. 1–6.
[53] I. Boldea and S. A. Nasar, *The Induction Machine Handbook*, 2nd ed. Boca Raton, FL, USA: CRC Press, 2010, pp. 28–30.
[54] T. Gundogdu, Z. Q. Mipo, J. C. Mipo, and S. Personnaz, "Influence of stator and rotor geometric parameters on rotor bar current waveform and performance of IMs," *J. Eng.*, vol. 2019, no. 17, pp. 3649–3654, doi: 10.1049/joe.2018.8244.
[55] (Nov. 25, 2021). *Material Market Priced*. [Online]. Available: https://www.lme.com/
[56] T. Gundogdu, Z. Q. Zhu, J. C. Mipo, and P. Farah, "Investigation of non-sinusoidal rotor bar current phenomenon in induction machines—Influence of slip and electric loading," in *Proc. Int. Conf. Elect. Mach. (ICEM)*, Lausanne, Switzerland, Sep. 2016, pp. 419–425.
[57] Y. Guan, Z. Q. Zhu, I. Afinowi, and J. C. Mipo, "Influence of machine design parameters on flux-weakening performance of induction machine for electrical vehicle application," *IET Electr. Syst. Transp.*, vol. 5, no. 1, pp. 43–52. Mar. 2015, doi: 10.1049/iet-est.2013.0058.

T. GUNDOGDU (Member, IEEE) received the B.Sc. degree in electrical education from Gazi University, Ankara, Turkey, in 2009, the M.Sc. degree in electrical engineering from Istanbul Technical University (ITU), Istanbul, Turkey, in 2012, and the Ph.D. degree in electronic and electrical engineering from The University of Sheffield, Sheffield, U.K., in 2018.

The topic of his Ph.D. thesis was advanced non-overlapping winding induction machine designs for electrical vehicle applications in collaboration with Valeo Powertrain Electric Systems. From 2010 to 2014, he was a Research Assistant at the ITU. From 2017 to 2018, he worked as a Researcher at The University of Sheffield's EMD Group in collaboration with IMRA Europe SAS. Since 2018, he has been an Assistant Professor at the Department of Electrical and Electronics Engineering, Hakkari University. His current major research interests include design, analysis, and control of novel electrical machines and magnetic sensors including induction, synchronous, permanent magnet brushless, reluctance, hybrid-excited, vernier permanent magnet, and resolvers for applications from electric vehicles through industrial to renewable energy.

Z. Q. ZHU (Fellow, IEEE) received the B.Eng. and M.Sc. degrees from Zhejiang University, Hangzhou, China, in 1982 and 1984, respectively, and the Ph.D. degree from The University of Sheffield, Sheffield, U.K., in 1991, all in electrical and electronic engineering.

Since 1988, he has been with The University of Sheffield, where he is currently a Professor with the Department of Electronic and Electrical Engineering, the Head of the Electrical Machines and Drives Research Group, the Royal Academy of Engineering/Siemens Research Chair, the Academic Director of the Sheffield Siemens Gamesa Renewable Energy Research Centre, the Director of the Midea Electrical Machines and Control Systems Research Centers, and the Director of the Sheffield CRRC Electric Drives Technology Research Centre. His current major research interests include the design and control of permanent-magnet brushless machines and drives for applications ranging from electrified transportation through domestic appliance to renewable energy. He is a fellow of the Royal Academy of Engineering and the IET, U.K. He was the recipient of 2019 IEEE Industry Applications Society Outstanding Achievement Award and the 2021 IEEE Nikola Tesla Award.

J. C. MIPO (Member, IEEE) received the Ph.D. degree in electrical engineering from Pierre and Marie Curie University, Paris, France, in 1998. Since 1998, he has been with Valeo Powertrain Electric Systems, Créteil, France, where he is currently the Advanced Technical Manager.